Quenching-driven equatorial depletion and limb asymmetries in hot Jupiter atmospheres: WASP-96b example

Maria Zamyatina[1]*, Duncan A. Christie[1,2], Eric Hébrard[1], Nathan J. Mayne[1],

Michael Radica[3], Jake Taylor[3,4], Harry Baskett[1], Ben Moore[1], Craig Lils[1], Denis Sergeev[1],

Eva-Maria Ahrer[2], James Manners[5], Krisztian Kohary[1] and Adina D. Feinstein[6]†

[1] *Department of Physics and Astronomy, Faculty of Environment, Science and Economy, University of Exeter, Exeter EX4 4QL, UK*
[2] *Max Planck Institute for Astronomy, Königstuhl 17, 69117 Heidelberg, Germany*
[3] *Institut Trottier de Recherche sur les Exoplanètes and Département de Physique, Université de Montréal, 1375 Avenue Thérèse-Lavoie-Roux,*
Montréal, QC, H2V 0B3, Canada
[4] *Department of Physics (Atmospheric, Oceanic and Planetary Physics), University of Oxford, Parks Rd, Oxford OX1 3PU, UK*
[5] *Met Office, Fitzroy Road, Exeter EX1 3PB, UK*
[6] *Laboratory for Atmospheric and Space Physics, University of Colorado Boulder, UCB 600, Boulder, CO 80309*

ABSTRACT

Transport-induced quenching in hot Jupiter atmospheres is a process that determines the boundary between the part of the atmosphere at chemical equilibrium and the part of the atmosphere at thermochemical (but not photothermochemical) disequilibrium. The location of this boundary, the quench level, depends on the interplay between the dynamical and chemical timescales in the atmosphere, with quenching occurring when these timescales are equal. We explore the sensitivity of the quench level position to an increase in the planet's atmospheric metallicity using aerosol-free 3D GCM simulations of a hot Jupiter WASP-96b. We find that the temperature increase at pressures of $\sim 10^4$–10^7 Pa that occurs when metallicity is increased could shift the position of the quench level to pressures dominated by the jet, and cause an equatorial depletion of CH_4, NH_3 and HCN. We discuss how such a depletion affects the planet's transmission spectrum, and how the analysis of the evening-morning limb asymmetries, especially within ~ 3–$5\,\mu m$, could help distinguish atmospheres of different metallicities that are at chemical equilibrium from those with the upper layers at thermochemical disequilibrium.

Key words: planets and satellites: atmospheres – planets and satellites: composition – planets and satellites: gaseous planets

1 INTRODUCTION

Hot Jupiters, i.e. close-in extrasolar gas giant planets, were, are and in the near future will be the best targets for exoplanet atmospheric characterisation. These planets host large and often anomalously inflated atmospheres (e.g., Tremblin et al. 2017; Komacek et al. 2022), which aid the detection and identification of atoms and molecules present in these atmospheres. One of the tools used to study hot Jupiter atmospheres is general circulation models (GCMs, e.g., Showman et al. 2009; Rauscher & Menou 2010; Dobbs-Dixon & Agol 2013; Mayne et al. 2014; Mendonça et al. 2016; Sainsbury-Martinez et al. 2019; Carone et al. 2020; Helling et al. 2020; Lee et al. 2021; Menou 2020). GCMs simulate the thermodynamic and chemical structure of a planetary atmosphere, and can predict different planetary climates depending on the choice of model parameters. One such parameter is the planet's atmospheric metallicity.

Atmospheric metallicity is the abundance of elements heavier than helium in a planetary atmosphere. Atmospheric metallicity affects many aspects of the planetary climate, e.g., the thermal structure,

atmospheric circulation and emitted flux (Drummond et al. 2018), however, the value of atmospheric metallicity for hot Jupiters is uncertain by several orders of magnitude (e.g., Welbanks et al. 2019). To correctly determine the atmospheric metallicity of a hot Jupiter, one, ideally, needs to fully understand the planet's observed thermochemical state. While achieving such an understanding is an active area of research, hot Jupiters that have "aerosol-free" limbs at observable pressures, meaning that the opacities of aerosols constituting condensate clouds and/or photochemical hazes contribute little to the planet's transmission spectrum, can aid such research. WASP-96b was historically considered one of "aerosol-free" hot Jupiters.

WASP-96b is a highly inflated hot Jupiter, with a mass of 0.48 ± 0.03 M_J and a radius of 1.20 ± 0.06 R_J (Hellier et al. 2014). It orbits a G8-type star at a distance of 0.0453 AU in 3.425 days, which results in it likely being tidally-locked and having an equilibrium temperature of 1285 ± 40 K (Hellier et al. 2014). WASP-96b was observed with transit photometry with the Transiting Exoplanet Survey Satellite (*TESS*, 0.60–1.00 µm, Yip et al. 2021; Nikolov et al. 2022) and the Infrared Array Camera on the Spitzer Space Telescope (*Spitzer*/IRAC, 3.6 and 4.5 µm, Yip et al. 2021; Nikolov et al. 2022) as well as with ground- and space-based transit spectroscopy with the FOcal Reducer/low dispersion Spectrograph 2 on the Very Large

---

Telescope Unit 1 (*VLT*/UT1/FORS2, 0.35–0.80 µm, Nikolov et al. 2018), the Inamori-Magellan Areal Camera and Spectrograph on the Baade-Magellan Telescope (*Magellan*/IMACS, 0.475–0.825 µm, McGruder et al. 2022), the Wide Field Camera 3 using G102 and G141 grisms on the Hubble Space Telescope (*HST*/WFC3 G102 and G141, 0.78–1.65 µm, Yip et al. 2021; Nikolov et al. 2022) and most recently JWST Near Infrared Imager and Slitless Spectrograph using the Single Object Slitless Spectroscopy mode (*JWST*/NIRISS/SOSS, 0.6–2.8 µm, Radica et al. 2023) as a part of the JWST Early Release Observations (ERO) program (Pontoppidan et al. 2022).

Evidence for the "aerosol-free" nature of WASP-96b is three-fold. (1) The WASP-96b *VLT*/UT1/FORS2 transmission spectrum exhibited a broad Na I line adsorption feature at ~0.50–0.75 µm (Nikolov et al. 2018), the presence of which was later independently confirmed by *Magellan*/IMACS observations (McGruder et al. 2022). (2) The WASP-96b *HST*/WFC3 G102 and G141 transmission spectrum showed a full H_2O absorption feature centered at ~1.4 µm (Yip et al. 2021; Nikolov et al. 2022), the presence of which was also independently confirmed by *JWST*/NIRISS/SOSS observations (Radica et al. 2023). The broadness of the observed Na I line feature suggested that the light transmitted through WASP-96b atmosphere was unimpeded by interactions with opacity sources other than Na, which would otherwise have obscured Na I wings or even its line core. That, in turn, meant that *VLT*/UT1/FORS2 and *Magellan*/IMACS observations probed a large range of the planet's atmospheric pressures and captured Na I adsorption line broadening (Hedges & Madhusudhan 2016). Similarly to Na I, the observation of a full and unmuted H_2O absorption feature suggested that H_2O was the only opacity source contributing to the spectrum at *HST*/WFC3 G102 and G141 and relevant *JWST*/NIRISS/SOSS wavelengths. (3) 1D forward and retrieval modelling based on the aforementioned WASP-96b pre-JWST transmission spectrum had consistently found WASP-96b's observed limbs to be "aerosol-free" (Nikolov et al. 2018; Welbanks et al. 2019; Alam et al. 2021; Nikolov et al. 2022; McGruder et al. 2022).

The "aerosol-free" status of WASP-96b has recently been put into question by the theoretical work of Samra et al. (2023) and observations made using *JWST*/NIRISS/SOSS (Radica et al. 2023; Taylor et al. 2023). Samra et al. (2023) explored the possibility of cloud formation in the atmosphere of WASP-96b using a hierarchy of forward and retrieval models. Their simulations predict that a mix of ≈40% silicate ($MgSiO_3[s]$, $Mg_2SiO_4[s]$, $Fe_2SiO_4[s]$, $CaSiO_3[s]$) and ≈40% metal oxide ($SiO[s]$, $SiO_2[s]$, $MgO[s]$, $FeO[s]$, $Fe_2O_3[s]$) clouds would dominate the limbs of WASP-96b at observable pressures and that there would be a slight asymmetry between the limbs, with the morning limb being cloudier. They proposed two scenarios that allow for Na I and H_2O features to be observed even in the presence of clouds. (1) WASP-96b could have a low vertical mixing efficiency, which would reduce the cloud top height whilst keeping the cloud base unchanged. (2) WASP-96b could have a high cloud particle porosity, which would reduce the cloud opacity by making the clouds optically thinner. Radica et al. (2023) and Taylor et al. (2023) reported tentative evidence for haze in the atmosphere of WASP-96b. According to Radica et al. (2023), the first *JWST* spectrum of WASP-96b contained three H_2O features centered at ~1.2, 1.4 and 1.8 µm, respectively, and a K feature at ~0.76 µm embedded into a Rayleigh scattering slope. Their analysis of this spectrum with three grids of 1D radiative-convective chemical equilibrium models revealed the following. (1) MnS[s] and $MgSiO_3[s]$ cloud formation, inferred from comparing their best-fitting planet-average so-

lar[1]-metallicity pressure-temperature profile to several cloud species' condensation curves, is possible, however the cloud top of such, assumed to be optically thick, clouds had to be located below the pressures observable during transit (at ~10^5 Pa). (2) The observed Rayleigh slope could be explained by either an enhanced Rayleigh scattering by small particles, i.e., possibly haze, or by a highly-pressure-broadened red wing of the Na I line. The degeneracy between an enhanced Rayleigh scattering and a high Na abundance had been pointed out previously (e.g., by Nikolov et al. 2018), but breaking this degeneracy in the case of WASP-96b would require an analysis of, e.g., a WASP-96b combined *VLT*/UT1/FORS2 and *JWST*/NIRISS/SOSS spectrum, which was outside the scope of their study. Taylor et al. (2023) extended the work of Radica et al. (2023) by interpreting WASP-96b *JWST*/NIRISS/SOSS observations using a combination of two 3D GCMs and four grids of 1D retrievals. Both participating GCMs, the SPARC/MITGCM and the Met Office UNIFIED MODEL (UM), were aerosol-free and were run for two scenarios: the SPARC/MITGCM with 1× and 10×solar[2] metallicity under the assumption of chemical equilibrium, and the UM with 1×solar[3] metallicity and under the assumption of chemical equilibrium or disequilibrium. The comparison of GCM-derived limb-average pressure-temperature profiles to cloud species' condensation curves revealed that all four GCM simulations predicted a thermal structure that permits MnS[s] cloud formation at both WASP-96b's limbs, with SPARC/MITGCM 1×solar simulation also allowing for high-altitude $Na_2S[s]$ clouds at the morning limb. $MgSiO_3[s]$ cloud formation was also possible at ≥10^5 Pa. The transmission spectra computed from GCM simulations generally agreed with the *JWST*/NIRISS/SOSS spectrum longward of 1.3 µm, but underestimated the observed transit depths shortward of 1.3 µm likely due to the lack of a scattering opacity source. That encouraged an investigation using atmospheric retrievals. All retrieval codes participating in the work of Taylor et al. (2023), CHIMERA, AURORA, PYRATBAY and POSEIDON, found that scenarios with inhomogeneous clouds and hazes were preferred over cloud-free ones, which was caused primarily by the detection of a Rayleigh scattering slope rather than of an opacity from a grey cloud top. All free retrieval codes recovered chemical species abundances that are consistent between the codes, with abundances from AURORA being: $\log_{10}(H_2O) = -3.59^{+0.35}_{-0.35}$, $\log_{10}(CO_2) = -4.38^{+0.47}_{-0.57}$, $\log_{10}(K) = -8.04^{+1.22}_{-1.71}$, which are generally consistent with a solar[4] metallicity and a solar CO (upper limit), except for CO_2, whose abundance is more consistent with its equilibrium abundance at 10×solar metallicity.

In addition to aerosol formation, other processes can alter the transmission spectrum of hot Jupiters atmospheres, e.g., transport-induced quenching (Moses 2014; Zahnle & Marley 2014), which we later refer to as "quenching" for simplicity. Quenching is a process that determines the boundary between the part of the atmosphere at chemical equilibrium and the part of the atmosphere at thermochemical (but not photothermochemical) disequilibrium. The location of this boundary, the quench level, depends on the interplay between the dynamical and chemical timescales in the atmosphere, with quenching occurring when these timescales are equal. The sensitivity of quenching to changes in a variety of stellar and planetary parameters was explored with pseudo-2D (Baeyens et al. 2021; Moses et al. 2022) and 3D (Drummond et al. 2020; Zamyatina et al. 2023) for-

---

ward models, however, the sensitivity of quenching to the metallicity increase has never been explored with a GCM.

Motivated by the uncertainty in WASP-96b's atmospheric metallicity, in this study we designed several 3D GCM simulations (Section 2) to help us do the following. (1) Explore how 3D GCM predictions of WASP-96b's atmospheric circulation (Section 3.1) and chemistry (Section 3.2) differ depending on the assumed metallicity and the assumed atmospheric thermochemical state, equilibrium or disequilibrium. (2) Explore how quenching responds to the metallicity increase, and causes an equatorial depletion of CH_4, NH_3 and HCN (Section 3.2.1) and limb asymmetries (Section 3.2.2). (3) Identify parts of the simulated WASP-96b transmission spectrum that are sensitive to the metallicity increase and disequilibrium chemistry (Section 3.3). Finally, we compare the observed and simulated WASP-96b transmission spectra (Section 3.4), and present our discussion and conclusions in Sections 4 and 5, respectively.

2 SIMULATIONS

We used the Met Office UNIFIED MODEL (UM) GCM with the same basic model setup as in Drummond et al. (2020) and Zamyatina et al. (2023). In brief, the dynamical core of our GCM solves the full, deep-atmosphere, non-hydrostatic equations of motion using a semi-implicit semi-Lagrangian scheme. The radiative transfer component of our GCM solves the two-stream equations in 32 spectral bands covering 0.2–322 μm and treats opacities using the correlated-k and equivalent extinction methods. Our opacity sources include the absorption due to H_2O, CO, CO_2, CH_4, NH_3, HCN, Li, Na, K, Rb, Cs and collision-induced absorption due to H_2-H_2 and H_2-He as well as Rayleigh scattering due to H_2 and He (see Goyal et al. (2020), for line list information). We chose a model grid resolution of 2.5° longitude by 2° latitude and 66 vertical levels equally spaced in height (covering pressures from ~2×10^7 Pa to ~1 Pa). While such a grid resolution is too coarse to resolve individual convective plumes, we let the non-hydrostatic core of our GCM remove convective instabilities at the grid scale and do not use a convection scheme. For the stellar spectrum we used the PHOENIX BT-Settl stellar spectrum (Rajpurohit et al. 2013) closely matching WASP-96 (Table 1), and for the planet — WASP-96b parameters from Hellier et al. (2014) (Table 2). We initialised our GCM simulations at rest with the dayside-average pressure-temperature profiles from the 1D radiative-convective-chemistry model ATMO (e.g., Tremblin et al. 2015; Drummond et al. 2016) adopting the same WASP-96 system parameters and assuming chemical equilibrium for the chemical species present in the Venot et al. (2012) chemical network. The intrinsic temperature at the bottom boundary of the model domain was assumed to be 100 K in both ATMO and the UM. Lastly, and contrary to the GCM simulations in Drummond et al. (2020), Zamyatina et al. (2023) and Taylor et al. (2023), we used a smaller filtering constant, K, set to 0.04, instead of previously used K = 0.16, to reduce the strength of longitudinal filtering of the horizontal wind (e.g., Mayne et al. 2017), i.e., effectively reducing diffusion, to prevent the loss of a considerable amount of axial angular momentum and the emergence of a retrograde equatorial jet, both discussed in detail in Christie et al. (in prep.). All GCM simulations were aerosol-free, and were run for at least 1000 Earth days to let the upper atmosphere (10^2-10^5 Pa) reach a pseudo-steady state dynamically, radiatively and chemically (Figs. A1-A2). All fields shown later in this paper were chosen to be averaged over the last 200 simulation days.

We performed two pairs of GCM simulations (i.e., four simulations

Table 1. WASP-96 parameters used in this study.

Parameter	Value	Unit
Type	G8	
Radius	7.30×10^8	m
Effective temperature	5500	K
Stellar constant at 1 au	1272.86	W m^{-2}
$\log_{10}$(surface gravity)	4.50	(cgs)
Metallicity	0.00	dex

Table 2. WASP-96b parameters used in this study. Two values are listed for parameters that change with changing metallicity.

Parameter	Value (for 1×, 10×solar)	Unit
Inner radius	8.39×10^7	m
Domain height	1.03×10^7	m
Semi-major axis	0.0453	au
Orbital period	3.4252602	Earth day
Rotation rate	2.12×10^{-5}	rad s^{-1}
Surface gravity	7.59	m s^{-2}
Specific gas constant	3516.29, 3164.69	J K^{-1} kg^{-1}
Specific heat capacity	1.26×10^4, 1.15×10^4	J K^{-1} kg^{-1}
Stellar irradiance	0.62×10^6	W m^{-2}
Effective temperature	1250	K

in total), exploring the sensitivity of the atmospheric structure of WASP-96b to the following:

(1) the assumed metallicity, 1× solar ([M/H] = 0) or 10× solar ([M/H] = 1); and
(2) the assumption about whether the entire atmosphere is at chemical equilibrium or allowing upper layers of the atmosphere to be at chemical disequilibrium. The simulations that assumed chemical equilibrium computed abundances of chemical species using the Gibbs minimisation scheme, and are later referred to as "equilibrium" simulations. The simulations that allowed for chemical disequilibrium computed the production and loss of chemical species present in the Venot et al. (2019) reduced chemical network, and are later referred to as "kinetics" simulations.

We did not include photochemistry into our kinetics simulations, meaning that these simulations take into account only disequilibrium thermochemistry. We also assumed gas-phase only composition in all simulations. Finally, our simulations included the calculation of alkali metal abundances during the simulation run time. Since the chemical kinetics of alkali metals is poorly known for H_2-rich atmospheres, alkali metals were not included into the chemical network used in our kinetics simulations. Instead, in both equilibrium and kinetics simulations, alkali metal abundances were computed using the parameterization of Amundsen et al. (2016), which takes alkali metals' monatomic/polyatomic transformation curves from Burrows & Sharp (1999) chemical equilibrium abundances and applies additional smoothing to these curves to avoid a step change in abundance. We plan to transition from using this parameterization to computing alkali metal abundances assuming chemical equilibrium in the near future.

3 RESULTS

3.1 Atmospheric circulation

Let us consider the atmospheric circulation and temperature of WASP-96b predicted at 10^3 Pa (Fig. 1a-d). As expected for any typi-

cal tidally-locked hot Jupiter, the dayside of the planet is hotter than the nightside, and the hot spot is shifted eastward from the substellar point by the zonal heat transport within the eastward equatorial jet. Both the metallicity increase (Fig. 1e-f) and disequilibrium thermochemistry (Fig. 1g-h) have an impact on the planet's thermodynamical structure, but an increase in metallicity alters this structure more than disequilibrium thermochemistry.

An increase in metallicity from [M/H] = 0 to [M/H] = 1 increases the day-night temperature contrast at 10^3 Pa. At [M/H] = 0 the day-night temperature contrast (dayside maximum minus nightside minimum) is ~500 K, while at [M/H] = 1 it is higher, mostly due to a higher dayside temperature, and is equal to ~800 K. This temperature contrast is accompanied by the difference in the maximum zonal-mean zonal wind speed (Fig. A3). This wind speed is ~0.5 km s^{-1} faster at [M/H] = 1 than at [M/H] = 0, whilst the jet occupies a similar part of the atmosphere — between ±40° latitude and down to ~3×10^5 Pa. Such a change in WASP-96b's thermodynamical structure with increasing metallicity occurs because as metallicity increases the mean molecular weight and opacity of the atmosphere increases while its specific heat capacity decreases (e.g., Drummond et al. 2018). The combined effect of these changes causes the atmosphere to experience a more compact flow structure and shallower heating, which together reduce the day-night heat transport, and cause the simulations with a higher metallicity to have an overall warmer dayside and a cooler nightside than the simulations with a lower metallicity.

An increase in metallicity from [M/H] = 0 to [M/H] = 1 also amplifies the thermal limb[5] asymmetry at 10^3 Pa. Given that a tidally-locked hot Jupiter typically has a colder morning limb and a warmer evening limb, our simulations predict that at 10^3 Pa WASP-96b's cold morning limb will be even colder (by up to 50 K) and the warm evening limb will be even warmer (by up to 100 K) at [M/H] = 1 than at [M/H] = 0. This results in the average evening minus morning limb temperature difference at 10^3 Pa being ~250 K at [M/H] = 0 and ~460 K at [M/H] = 1. The thermal limb asymmetry at other pressure levels is shown in Fig. A4.

Disequilibrium thermochemistry changes the predicted thermal structure of WASP-96b at 10^3 Pa mostly near the morning limb. The morning limb is influenced by the circulation in the Rossby gyres (e.g., Showman et al. 2020) that transport colder gas from the nightside to the dayside in the equatorial region and warmer gas from the dayside to the nightside in the polar regions. At both metallicities our kinetics simulations predict lower temperatures inside the Rossby gyres than those in the equilibrium simulations. As a result, the morning limb in the kinetics simulations is colder up to 30 K at [M/H] = 0 and 120 K at [M/H] = 1 (i.e. comparable in magnitude to the thermal limb asymmetry due to the metallicity increase).

3.2 Chemical structure

The predicted chemical structure of WASP-96b changes considerably due to both the metallicity increase from [M/H] = 0 to [M/H] = 1 and disequilibrium thermochemistry. Different chemical species respond differently to both effects, and if we compare species' sensitivities to these effects, CO, H_2O and CO_2 are more sensitive to the metallicity increase, while CH_4, NH_3 and HCN are sensitive to both.

As metallicity increases, both equilibrium and kinetics simulations predict that the abundance of CO, H_2O and CO_2 increases by up to two orders of magnitude throughout the entire atmosphere. However, the spatial distribution of these species does not appreciably change: CO and H_2O stay predominantly vertically and horizontally uniform, while CO_2 follows the temperature structure by being more abundant at lower temperatures.

The response of CH_4, NH_3 and HCN to the metallicity increase and disequilibrium thermochemistry is more complex (Fig. 2 for CH_4 at 10^3 Pa). As metallicity increases, the equilibrium simulations predict a decrease in CH_4 on the dayside and the evening limb and an increase on the nightside and the morning limb (Fig. 2e). For NH_3 and HCN, however, the equilibrium simulations predict an increase in their abundance throughout the entire atmosphere, with this increase being larger on the nightside and the morning limb, similarly to CH_4. Contrary to the equilibrium simulations, the kinetics simulations predict an overall decrease in CH_4, NH_3 and HCN at $\leq 10^5$ Pa when metallicity is increased (Fig. 2f). Meanwhile, disequilibrium thermochemistry alters CH_4 distribution away from that at chemical equilibrium differently at different metallicities. At [M/H] = 0, disequilibrium thermochemistry increases CH_4 abundance outside of the Rossby gyres whist decreasing it inside the gyres, overall leading to a more horizontally homogeneous CH_4 distribution (Fig. 2b). At [M/H] = 1, however, the same zonal homogenisation is occurring (Fig. 2d), but the equatorial depletion in CH_4 barely noticeable at [M/H] = 0 (better seen in Fig. 4b) becomes more prominent at [M/H] = 1. This phenomenon, the equatorial depletion of CH_4, also occurring for NH_3 and HCN (Figs. A5-A6b,d), is caused by quenching.

3.2.1 Quenching-driven equatorial depletion

To understand the mechanism of CH_4, NH_3 and HCN quenching-driven equatorial depletion, we manually identified the pressure level at which each of these species quenches for the first time, i.e. has their deepest quench level. To illustrate the mechanism and relate the quench level information to observations in primary transit, we show the CH_4, NH_3, HCN (and CO_2) quench level positions in the terminator plane during mid-transit overlaid onto the temperature, zonal wind (Fig. 3) and chemical species abundance fields (Fig. 4b,d for CH_4 and Figs. A5-A7b,d for other species). By presenting the data this way we effectively show where the part of the atmosphere geometrically seen in mid-transit splits into two regions from the point of view of each of these three species. One region experiences chemical equilibrium and is located inside the quench-level contours (at higher pressures), and the other region experiences thermochemical disequilibrium and is located outside the quench-level contours (at lower pressures).

CH_4, NH_3 and HCN quench at different pressures at different metallicities, and the pressure level at which their quenching occurs changes with latitude. At [M/H] = 0, all three species quench at ~10^5–10^6 Pa, across the entire terminator plane. At [M/H] = 1, however, their equatorial to mid-latitude (within about ±45° latitude) quench levels are located at lower pressures, ~10^3–10^4 Pa, than elsewhere, which places these quench levels closer to the region of the equatorial jet. Such a protrusion of quench levels into the jet region suggests that the time scales of dynamical mixing (τ_{dyn}) and species' chemical conversion (τ_{chem}), which when in balance cause quenching (e.g., Moses et al. 2011), change with latitude. If we consider τ_{dyn} only in the zonal direction (as is shown in Fig. 3c,d), in the [M/H] = 1 kinetics simulation τ_{dyn} shortens equatorward and with decreasing pressure following the increase in the zonal wind speed,

---

[5] Limb here is defined as a pressure-latitude cross-section that divides a planetary atmosphere into a day-lit side and a dark night side. In our simulations, this cross-section aligns with longitudes 90°E and 270°E, with the substellar point being at 180°E.

WASP-96b: latitude-longitude cross section at 10^3 Pa
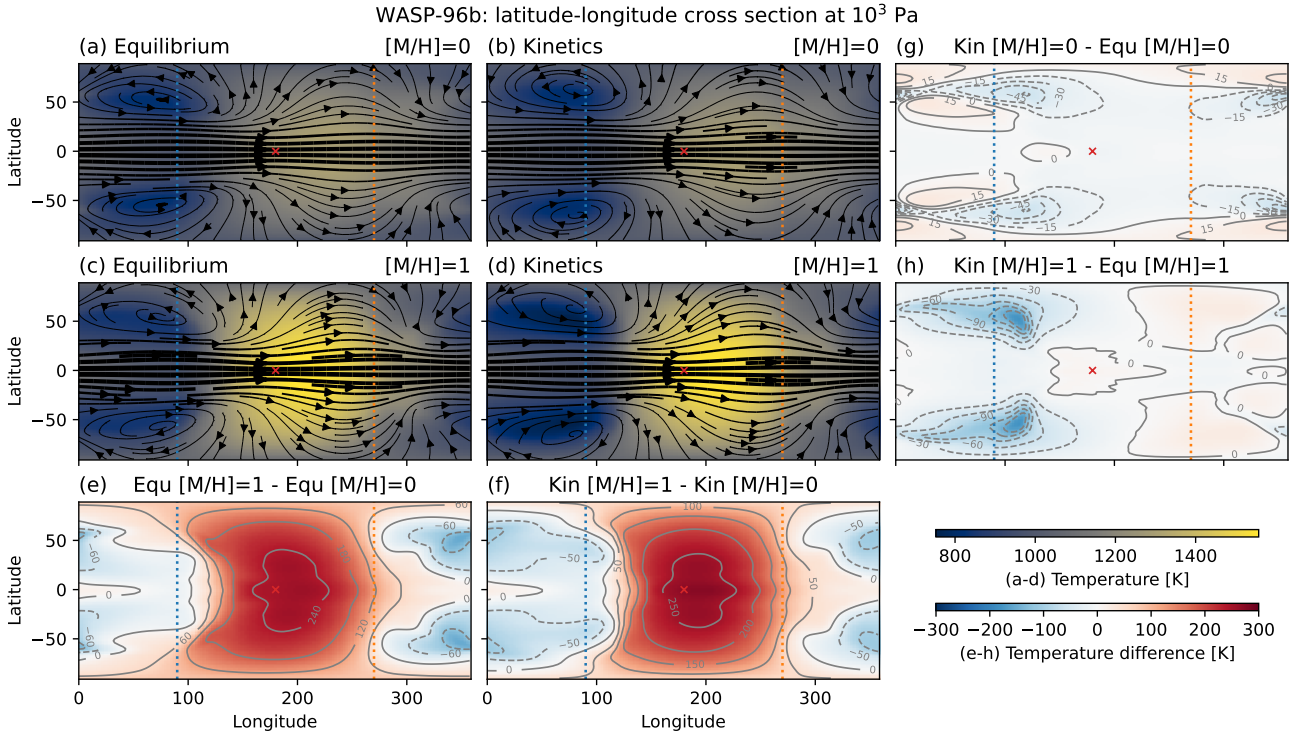
Figure 1. Temperature and horizontal wind streamlines at 10^3 Pa in the WASP-96b equilibrium and kinetics simulations assuming [M/H] = 0 or [M/H] = 1. Panels (a-d) show the general circulation pattern: the equatorial jet and mid-latitude Rossby wave crests and troughs. Panels (a-d) share a colour scale (the top one in the bottom right of the figure), and a streamline scale, with the width of streamlines scaled with horizontal wind speed and normalised to the maximum horizontal wind speed within 10^2-10^5 Pa (i.e., effectively inside the equatorial jet) between all four simulations. Panels (e-f) show the difference caused by an increase in metallicity, and (g-h) the difference caused by disequilibrium thermochemistry. Panels (e-h) share a colour scale (the bottom one in the bottom right of the figure). Red crosses mark the substellar point, and vertical dotted lines mark the morning (90°E in blue) and evening (270°E in orange) limb.

WASP-96b: latitude-longitude cross section at 10^3 Pa
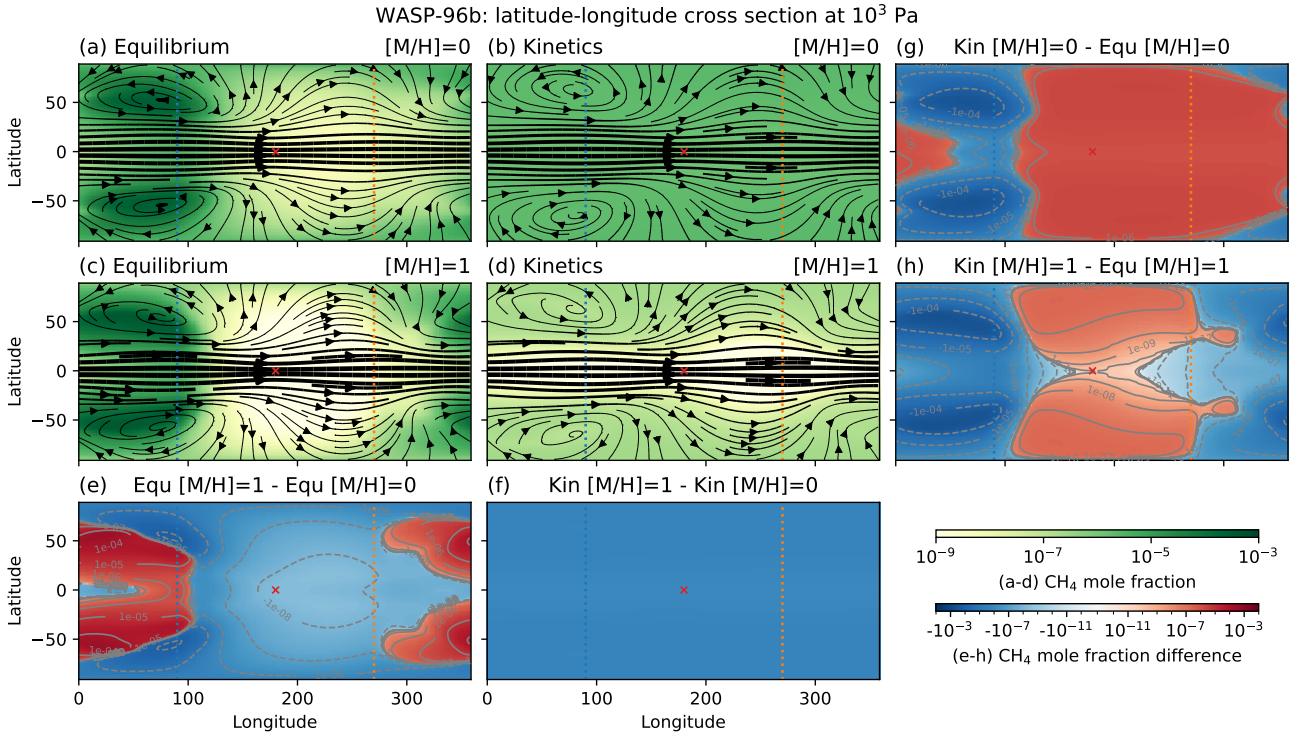
Figure 2. As in Fig. 1 but for CH_4 mole fraction.
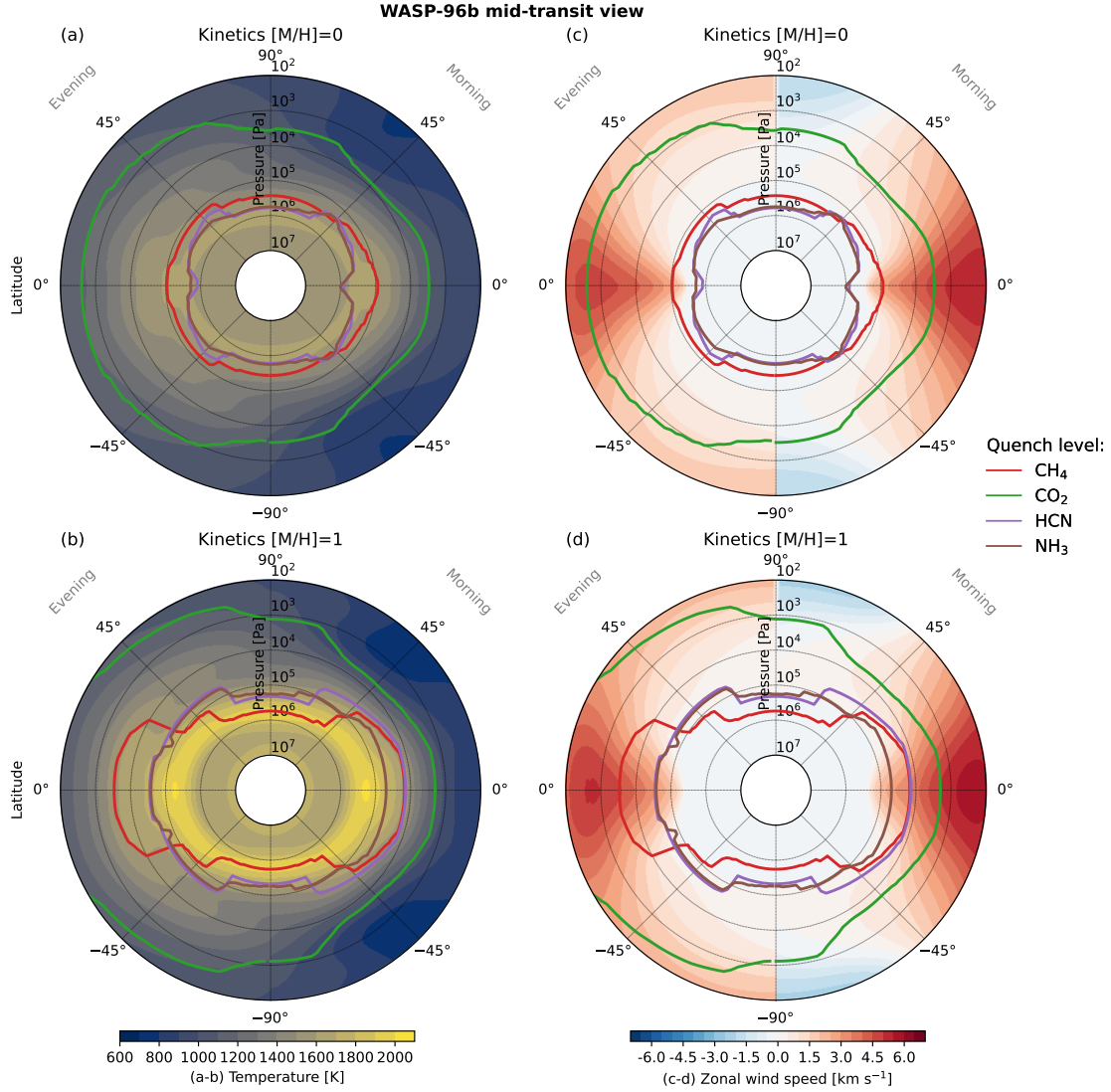
Figure 3. Pressure-temperature cross-sections through WASP-96b's terminator ("mid-transit view") in the kinetics simulations assuming [M/H] = 0 or [M/H] = 1. Left column shows the thermal structure in each simulation, and right column shows zonal wind speed. Coloured lines show the location of chemical species' quench points: CH_4 in red, CO_2 in green, HCN in purple and NH_3 in brown. All panels show variable distributions at longitudes 90°E and 270°E exactly (not the average over the opening angle).

while τ_{chem} reacts to changes in the speed of the prevailing species' conversion pathways.

The factor that enables and strengthens CH_4, NH_3 and HCN quenching-driven equatorial depletion is the increase in temperature at ~10^4–10^7 Pa due to an increase in atmospheric metallicity. These pressure levels of WASP-96b's simulated atmosphere are hotter at [M/H] = 1 than at [M/H] = 0, which pushes isotherms critical for CH_4, NH_3 and HCN chemistry, ~1400–1600 K (Moses et al. 2011; Baeyens et al. 2021), to lower pressures into the region of the equatorial jet. This, in turn, exposes gas close to chemical equilibrium to a sharp gradient in the zonal wind speed, forcing species' quench levels, i.e. the location at which τ_{dyn} equals each of the species' τ_{chem}, to shift to lower pressures. The [M/H] = 1 kinetics case additionally shows that these quench level shifts required to achieve $\tau_{dyn} = \tau_{chem}$ not only change with latitude, but also differ between the limbs. The CH_4 quench levels protrude more into the jet region at the evening limb than at the morning limb, while NH_3 and HCN quench lev-

els do the opposite. This leads to another phenomenon, CH_4, NH_3 and HCN quenching-driven limb asymmetry in equatorial depletion, which is the asymmetry in the magnitude and spatial extent of said depletion between the limbs.

The signs of CH_4, NH_3 and HCN quenching-driven equatorial depletion were present in the UM simulations of HD 189733b and HD 209458b (Drummond et al. 2020; Zamyatina et al. 2023) performed with the Venot et al. (2019) chemical network, and recently were also reported to be present in the Exo-FMS simulations of HD 189733b and WASP-39b (Lee et al. 2023) performed with the Tsai et al. (2022) "mini-chemical" network. There *are* differences between the UM and Exo-FMS HD 189733b CH_4, NH_3 and HCN quenched distributions, and while these particular simulations are not directly comparable (because Exo-FMS simulations did not have the coupling between the kinetics-driven changes in species abundances and radiative transfer), in the future it is important to explore the
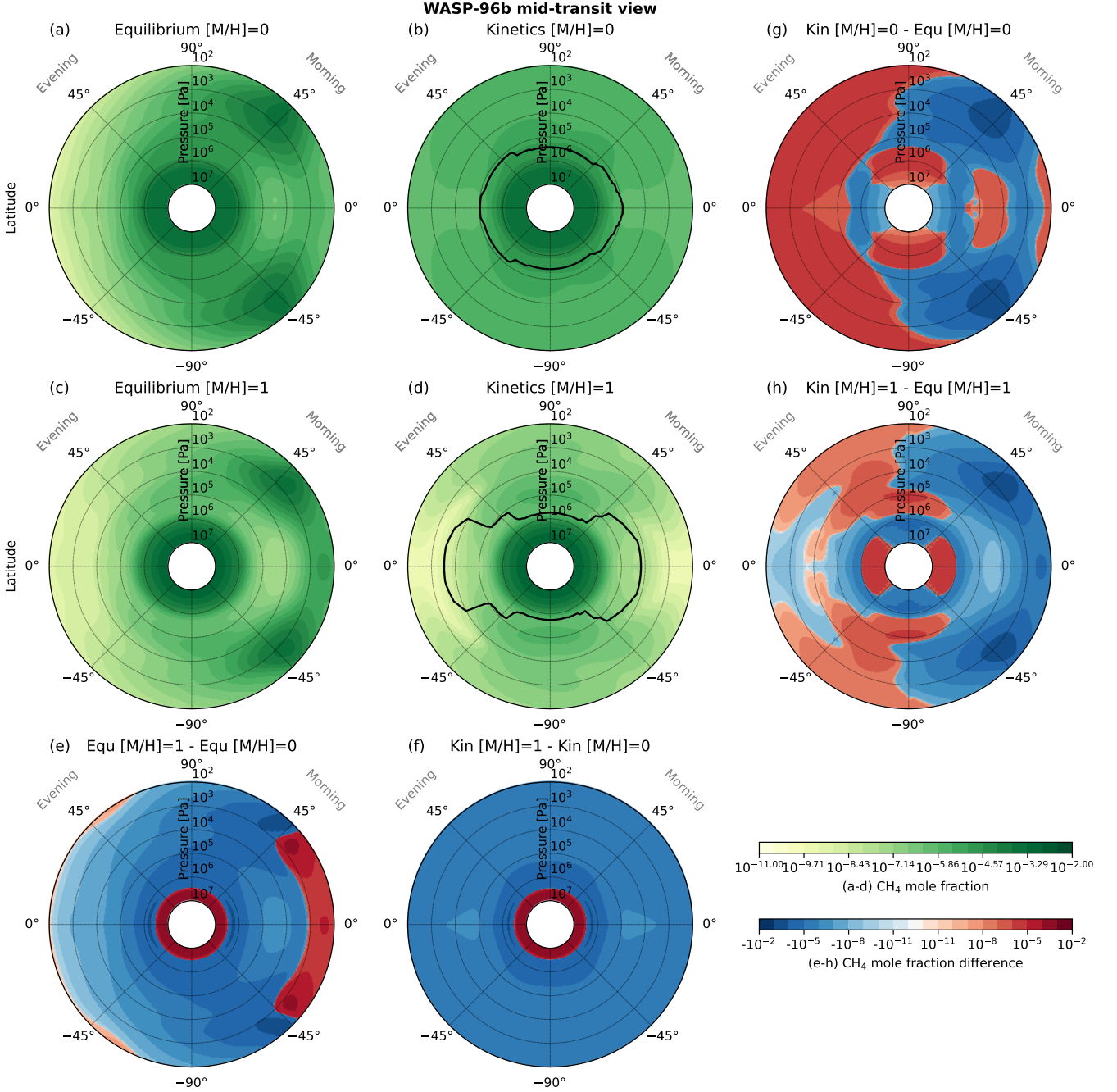
Figure 4. Pressure-CH$_4$ cross-sections through WASP-96b's limb ("mid-transit view") according to the equilibrium and kinetics simulations assuming [M/H] = 0 or [M/H] = 1. Panels (a-d) show CH$_4$ distribution in each simulation. Panels (e-f) show the difference caused by an increase in metallicity, and (g-h) the difference caused by disequilibrium thermochemistry. Panels (a-d) and (e-h) share the top and bottom colour scale in the bottom right of the figure, respectively. The black thick lines in panels (b) and (d) indicate the location of CH$_4$ quench level. All panels show variable distributions at longitudes 90°E and 270°E exactly (not the average over the opening angle).

process of quenching with different GCMs and estimate the "GCM uncertainty error bar" (Fauchez et al. 2022) for this process.

3.2.2 Quenching-driven limb asymmetries

Limb asymmetry is an asymmetry in characteristics of a planetary atmosphere between parts of its western and eastern hemispheres

observable in primary transit. The western part is often referred to as the morning (or leading) limb, as it is the region where atmospheric characteristics adjust from night to day conditions, while the eastern part, or the evening (or trailing) limb, is where they adjust from day to night conditions. Limb asymmetries were first detected in the atmospheres of the ultra-hot Jupiters WASP-76b and WASP-189b using high-resolution cross-correlation spectroscopy (Ehrenreich et al.

2020; Prinoth et al. 2022; Kesseli et al. 2022), and were recently found in the atmosphere of the hot Jupiter WASP-39b via the analysis of its *JWST* transit light curves (Rustamkulov et al. 2023, Espinoza et al. (in review), Delisle et al. (submitted)).

To correctly interpret observations of limb asymmetry, one needs to consider the drivers of limb asymmetry (e.g., Savel et al. 2023). One of the primary drivers of limb asymmetry is the temperature contrast between the limbs. The higher temperatures of the evening limb cause its atmospheric scale height to be larger than that of the morning limb, which leads to the evening-limb's transit depths being larger than those of the morning limb (Pluriel 2023). Another driver of limb asymmetry is the opacity contrast between the limbs. This opacity contrast could be caused by a multitude of processes, e.g., cloud (Line & Parmentier 2016; Powell et al. 2019) or haze formation (Steinrueck et al. 2021) or photochemistry (Tsai et al. 2023). In this study, we report how quenching changes the planet's limb opacity from that at chemical equilibrium, and how the associated evening-morning limb opacity contrast also changes depending on the assumed metallicity. For transmission spectra, we specifically focus on the mid-transit. We use the methodology of Lines et al. (2018) and Christie et al. (2021) to calculate the full, morning and evening limb transmission spectra, with the morning and evening limb spectra computed in the same way as the full limb spectra except that the given limb is mirrored to provide an appropriate planetary radius for the whole planet. The abundances of radiatively active species, H_2O, CO, CO_2, CH_4, NH_3, HCN, Li, Na, K, Rb, Cs, H_2 and He, are taken directly from the simulations, allowing for the abundances used in transmission spectra post-processing to be consistent with the chemistry used in the simulations.

According to our simulations, quenching alters the limb distribution of all chemical species, including those of CH_4, CO, CO_2, H_2O, NH_3 and HCN (Figs. 4g-h, A5-A9g-h, with vertical profiles shown in Figs. A10-A15). While the magnitude and location of these alterations varies amongst species, the general trend is that species that quench deeper in the atmosphere (e.g., CH_4, NH_3, HCN), as opposed to those that quench in the upper atmosphere (e.g., CO_2) or do not quench at all (e.g., OH or any other free radical), have a substantially more zonally-uniform limb distribution than that predicted at chemical equilibrium. For example, in the equilibrium simulations CH_4 is abundant in the cold Rossby gyres at the morning limb and is depleted in the warmer upper-atmosphere regions elsewhere, while in the kinetics simulations CH_4 limb distribution is zonally uniform, including the region of its equatorial depletion. In contrast to CH_4, CO_2 quenched limb distribution is similar to that at chemical equilibrium. This is because CO_2 quenches at much lower pressures than CH_4, which leaves a large part of CO_2 limb distribution untouched by quenching, especially at the morning limb, and instead determined by chemical equilibrium.

To understand if quenching-driven changes in the limb distributions of CH_4, NH_3, HCN and CO_2 could help distinguish aerosol-free atmospheres at chemical equilibrium from those at thermochemical disequilibrium, we calculated the evening minus morning limb transit depth differences caused by all and individual opacity sources separately (Fig. 5, with limb transit depth differences due to all opacity sources shown together in Fig. 6d). We find that these evening-morning limb differences vary with wavelength and across simulations. The main contributors to these differences are Rayleigh scattering (shortward of ~0.5 μm), Na and K absorption (within ~0.5–0.9 μm), and H_2O absorption (longward of ~0.9 μm). All the main contributors have a higher opacity at the evening limb than at the morning limb due to a higher temperature at the evening limb. Meanwhile, the contribution of other opacity sources to the

evening-morning limb differences changes between simulations. The contribution of CH_4 changes the most. In the equilibrium simulations, CH_4 has an opposite in sign and comparable to H_2O limb contrast, which is large enough to diminish the cumulative limb contrast of all opacity sources at wavelengths where CH_4 strongly absorbs. In the kinetics simulations, however, CH_4 limb contrast is mostly smaller than that of H_2O, yet it changes with metallicity: at [M/H] = 0 CH_4 is abundant and there is more of it at the evening limb, while at [M/H] = 1 CH_4 is depleted and there is a similar amount of it at both limbs. At around ~3.32 μm, CH_4 strongest absorption line in the infrared, the CH_4 limb contrast in the [M/H] = 0 kinetics simulation is comparable to that of H_2O, which causes the cumulative limb contrast of all opacity sources to increase around that wavelength.

The limb distribution of CO_2 also changes enough amongst our simulations to modify the evening-morning limb transit depth differences. Specifically, if we compare these differences at around ~4.23 μm, CO_2 strongest absorption line in the infrared, [M/H] = 0 simulations suggest that the abundance of CO_2 is low enough comparative to that of H_2O, so that the CO_2 limb contrast does not modify the cumulative limb contrast. However, [M/H] = 1 simulations show that the CO_2 abundance becomes high enough to be comparable to that of H_2O, and as a result the CO_2 limb contrast causes a dip in the cumulative limb contrast at around ~4.23 μm.

3.3 Parts of transmission spectrum sensitive to metallicity and quenching

Metallicity- and quenching-driven changes in the predicted atmospheric structure of WASP-96b translate into a number of differences in the planet's simulated transmission spectra (Figs. 5-6, A16-A17). To discuss these differences, we show our simulated spectra in five more different ways: (1) the full limb (morning plus evening) spectra (Fig. 6a), (2) the morning and evening limb spectra (Figs. 6b, A17), (3) the difference in the full limb spectra due to disequilibrium thermochemistry (Fig. 6c), (4) the difference between evening and morning limb spectra (Fig. 6d), and (5) the contributions of individual opacity sources to the full limb spectra (Fig. A16).

In the case of the full limb spectra, spectral differences caused by disequilibrium thermochemistry occur longward of the H_2- and He-induced Rayleigh scattering slope, with the largest difference being at around ~3.32 μm. Around that particular wavelength, the quenching-driven changes in CH_4, an enhancement at [M/H] = 0 and a depletion at [M/H] = 1, causes transit depths from [M/H] = 0 kinetics simulation to be ~300 ppm *larger* than those from [M/H] = 0 equilibrium simulation (Fig. 6c). Meanwhile, the corresponding transit depths from [M/H] = 1 kinetics simulation are ~100 ppm *smaller* than those from [M/H] = 1 equilibrium simulation. Such a difference in the sign of the change in CH_4 3.32 μm feature with increasing metallicity due to disequilibrium thermochemistry has two consequences. One, the CH_4 3.32 μm feature is a more powerful gauge of metallicity for hot Jupiter atmospheres at thermochemical disequilibrium than for atmospheres at chemical equilibrium. Two, for WASP-96b the presence of that feature in the planet's full limb transmission spectrum (Fig. 6a) would support a scenario of a lower, [M/H] = 0 metallicity atmosphere at thermochemical disequilibrium, rather than one of the other three scenarios considered in this study. The same argument is true for CH_4 7.70 μm and NH_3 10.37 μm features, but the metallicity- and quenching-driven changes in these features are smaller relative to those of CH_4 at 3.32 μm. CO_2 4.23 μm and 14.95 μm features, while also affected by the metallicity change and quenching, are less powerful in uniquely characterising hot Jupiter atmospheric metallicity. CO_2 4.23 μm feature is present in all our scenarios and only
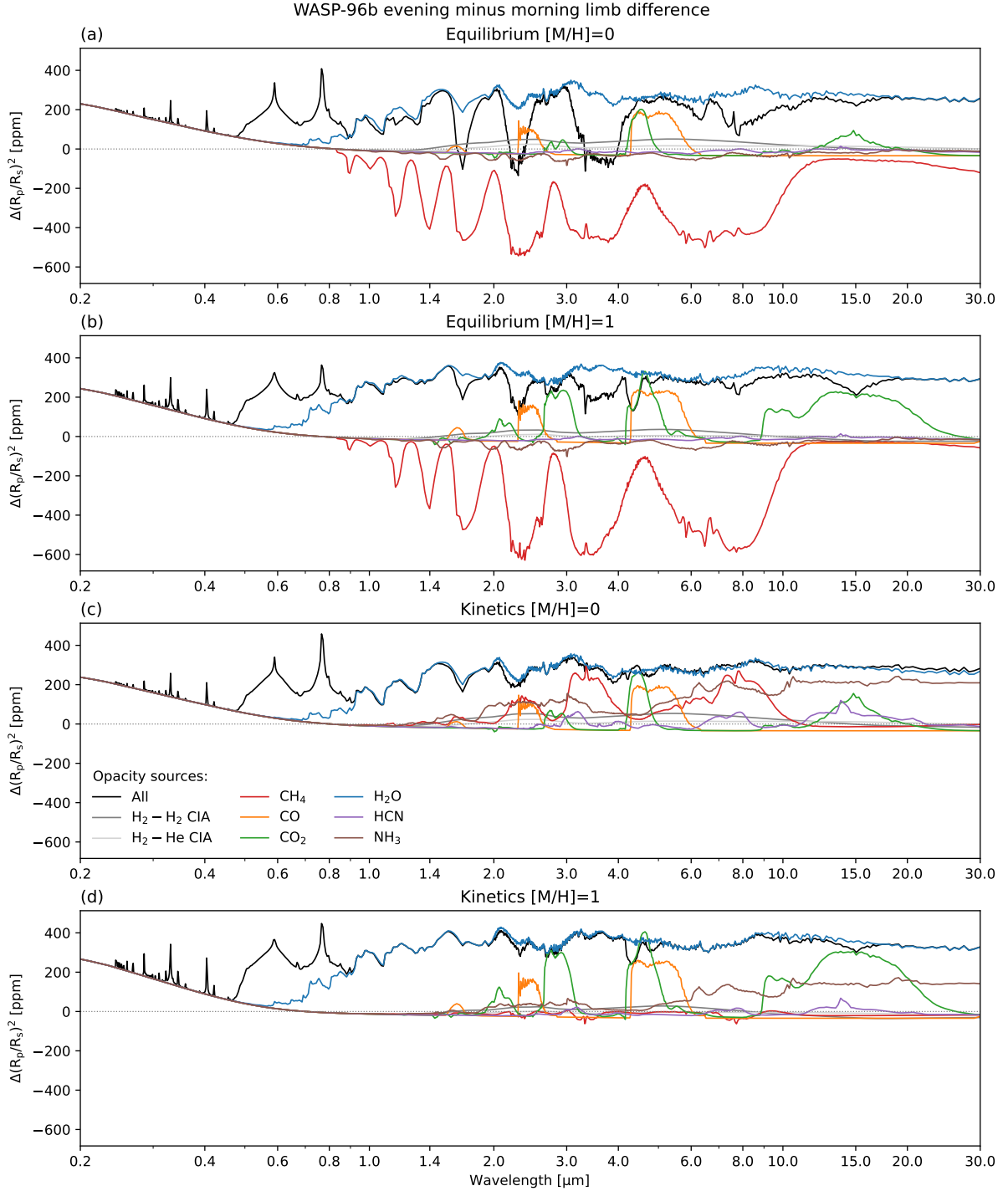
Figure 5. Contributions of individual opacity sources to the difference between evening and morning limb transmission spectra (evening minus morning) according to the WASP-96b equilibrium and kinetics simulations assuming [M/H] = 0 or [M/H] = 1. Faint grey dotted lines indicate the location of zero to better guide the eye.

the size of the feature is modified (Fig. A16). CO_2 14.95 μm feature, while present only at [M/H] = 1, is broad and is competing with a strong H_2O absorption. That means that putting information about CO_2 features into the context of surrounding wavelengths is critical for a correct identification of atmospheric metallicity.

In the case of the evening-morning limb asymmetries, spectral differences caused by the metallicity increase from [M/H] = 0 to

[M/H] = 1 and disequilibrium chemistry are comparable in size. The evening limb transit depths are ∼100-400 ppm larger than those of the morning limb in all our simulations except for the [M/H] = 0 equilibrium one (Fig. 6d). In that particular simulation, the transit depths for the evening limb are ∼100 ppm smaller than those of the morning limb around CH_4 1.67, 2.37, 3.21, 3.32 and 3.42 μm features. This sign reversal for the evening-morning limb difference is unique to

this simulation from our set of four simulations, and is caused by the fact that a higher than in any other scenario morning limb's CH_4 abundance and the resulting CH_4 limb contrast (Fig. 5) outweighs the temperature limb contrast present in this simulation. A similar argument is true for CH_4 7.40 and 7.70 µm features, but the lower pressure regions of the atmosphere sampled at these wavelengths do not have a strong enough CH_4 limb contrast to counteract the temperature limb contrast. While the analysis above helps separate the [M/H] = 0 equilibrium scenario from the other three considered in this study, distinguishing between both kinetics simulations and [M/H] = 1 equilibrium simulation is more difficult. At most wavelengths an increase in metallicity causes an offset between the evening-morning limb differences from the respective equilibrium and kinetics simulations, while offsets are known to be challenging to interpret if wavelength coverage is non-continuous (e.g., Carter et al., in review). Another difficulty is that different scenarios could produce similar in amplitude and shape evening-morning limb differences, for example, [M/H] = 0 kinetics and [M/H] = 1 equilibrium simulations within ~1.6–3.0 µm and ~5.0–7.0 µm (Fig. 6d). However, ~3.0–5.0 µm is the region where all four of our simulations predict *different in amplitude and shape* evening-morning limb differences, caused by the differences in H_2O, CH_4 and CO_2 (see Section 3.2.2). This makes the ~3.0–5.0 µm region the most powerful region for distinguishing atmospheres at chemical equilibrium from those at thermochemical disequilibrium and uniquely identifying their metallicity.

3.4 Comparison to existing observations

We compare an ensemble of the observed transmission spectra of WASP-96b from Nikolov et al. (2022), McGruder et al. (2022) and Radica et al. (2023) (the latter at R≈125) to our simulated spectra (Fig 7). Following Radica et al. (2023), we offset Nikolov et al. (2022)'s *VLT*/UT1/FORS2 and *HST*/WFC3 G102 and G141 spectra relative to the *JWST*/NIRISS/SOSS spectrum by +400 ppm and +200 ppm, respectively. We also offset McGruder et al. (2022)'s *Magellan*/IMACS-only spectrum by +1200 ppm relative to *JWST*/NIRISS/SOSS. Using the least squares method and the combined Nikolov et al. (2022)'s *VLT*/UT1/FORS2 and *HST*/WFC3 G102 and G141 and Radica et al. (2023)'s *JWST*/NIRISS/SOSS data, we fitted for offsets between the observed and simulated spectra, with these offsets resulting to be -1035 ppm and -1378 ppm for [M/H] = 0 and [M/H] = 1 pairs of simulations, respectively.

None of our simulated spectra match the existing observations perfectly, however this imperfection reveals the following:

(1) The 1.30–2.15 µm region is the only region where the transit depths predicted by all UM simulations stay mostly within the observational uncertainties. This is also the region where all simulated spectra differ the least, and show that the main contributor to the opacity is H_2O. Both of these factors suggest that all our simulations are consistent with WASP-96b's atmosphere having H_2O.

(2) For 0.35–0.60 µm, the spectra from our [M/H] = 0 simulations agree better with the *VLT*/UT1/FORS2 observations, however because we applied an offset of +400 ppm to the *VLT*/UT1/FORS2 data further interpretation is difficult.

(3) The 0.60–1.30 µm region is the region where K and H_2O absorption features predicted by the UM are not muted enough compared to observations. This is consistent with the presence of a scattering haze in WASP-96b's atmosphere.

(4) The 2.15–2.80 µm region is the region where the observed and all our simulated spectra broadly agree. However, because the observed transit depths vary a lot with wavelength, the identification of the best theoretical scenario is difficult.

(5) At 3.6 µm, all UM simulations predict transit depths that are within the uncertainty of the transit depth observed in this *Spitzer*/IRAC channel.

(6) At 4.5 µm, all UM simulations predict larger transit depths than the one observed in this *Spitzer*/IRAC channel.

Overall, our simulated WASP-96b transmission spectra are rather similar at the wavelengths that have been already observed, so observing WASP-96b at longer wavelengths, where our predicted spectra diverge more, would help better constrain WASP-96b's atmospheric metallicity.

4 DISCUSSION

The question of observability of the evening-morning limb asymmetries in hot Jupiter atmospheres has been of interest for some time from both the theoretical (e.g., Fortney et al. 2010; Kempton et al. 2017; Powell et al. 2019; Helling et al. 2020; MacDonald et al. 2020) and observational (e.g., von Paris et al. 2016; Espinoza & Jones 2021; Grant & Wakeford 2023) points of view. Early GCM aerosol-free simulations of Fortney et al. (2010) of the atmosphere of the hot Jupiter HD 189733b predicted that at [M/H] = 0 and chemical equilibrium the morning and evening hemisphere spectra of that planet would be different, with CH_4 absorption features being larger in the morning hemisphere spectra than the evening hemisphere spectra. When the GCM used in Fortney et al. (2010) included a simple representation of disequilibrium thermochemistry through the chemical relaxation scheme of Cooper & Showman (2006), however, the spectra of both hemispheres became almost identical, with large CH_4 absorption features being present in both hemispheres' spectra due to the homogenisation of CH_4 abundances by vertical mixing. Their results qualitatively agree with our results from WASP-96b [M/H] = 0 and [M/H] = 1 equilibrium and [M/H] = 0 kinetics simulations, respectively. However, our [M/H] = 1 kinetics simulation additionally suggests that while the spectra of both limbs are almost identical due to the homogenisation of quenched species abundances by horizontal and vertical mixing, quenching-driven equatorial depletion of CH_4 causes CH_4 absorption features in both limbs' spectra to be small and possibly undetectable (Fig. A17). The impact of aerosols on the limbs' spectra of hot and ultra-hot Jupiters was explored by Kempton et al. (2017) and Powell et al. (2019), who also estimated the size of the combined effect of the temperature and aerosol opacity contrast between the limbs on the limbs' spectra. Kempton et al. (2017)'s simulations with a GCM coupled (but not radiatively) to a phase-equilibrium cloud model predicted that at [M/H] = 0 the differences between the morning and evening limb spectra of the ultra-hot Jupiter WASP-121b could be ~100 ppm at ~0.7–5.0 µm, rising up to 400 ppm at optical wavelengths in the case of a purely Rayleigh scattering aerosol. Powell et al. (2019)'s simulations with a size-distribution-resolving cloud microphysics 1D model suggested that for hot Jupiters with equilibrium temperatures of 1800–2100 K and [M/H] = 0, limb differences could be ~600 ppm at ~0.7–30.0 µm, rising up to ~700–1200 ppm in the optical. Our aerosol-free WASP-96b GCM simulations forecast similar in magnitude evening-morning limb differences, ~100–400 ppm at 0.2–30 µm, to those of Kempton et al. (2017) and Powell et al. (2019), with quenching contributing up to ~300 ppm at [M/H] = 0 and ~200 ppm at [M/H] = 1 at ~2.0–30.0 µm to these differences (Fig. 6d). From an observational perspective, several studies proposed techniques for detecting limb
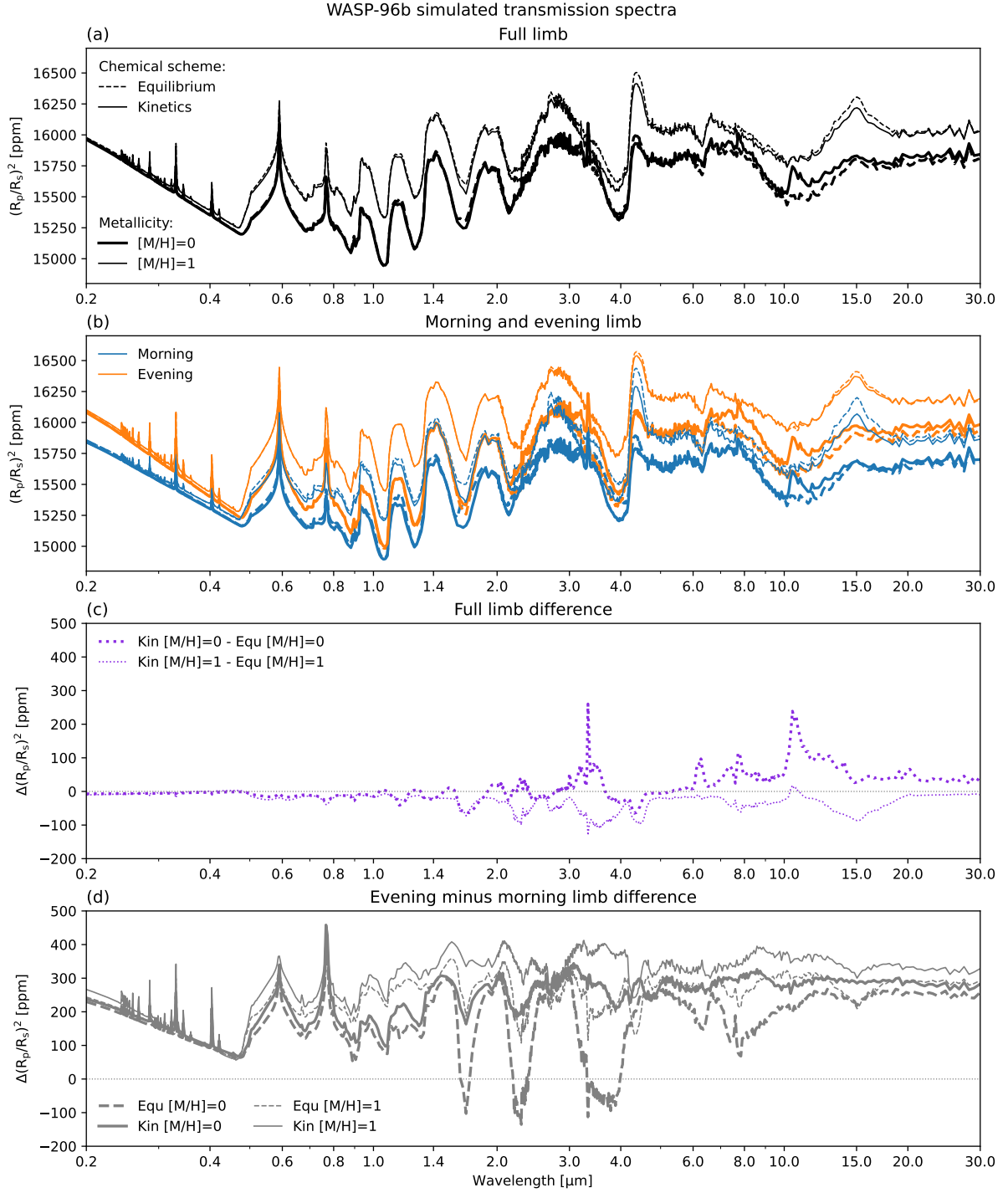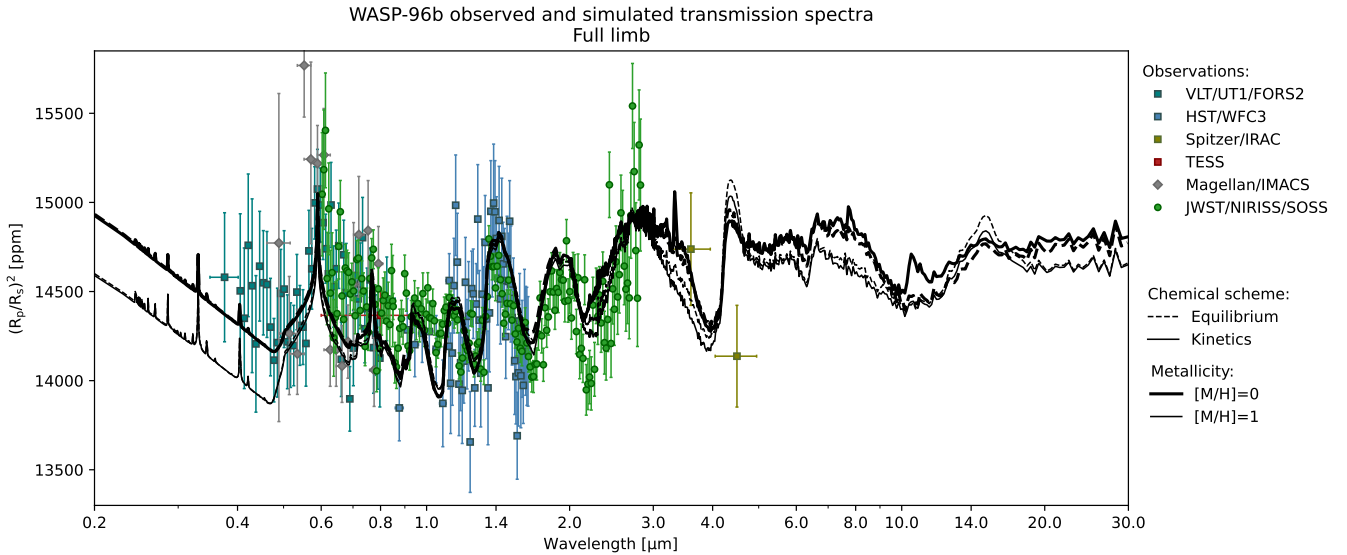
Figure 6. WASP-96b transmission spectra predicted by the Met Office UNIFIED MODEL equilibrium and kinetics simulations assuming [M/H] = 0 or [M/H] = 1. Panel (a) shows the full limb (morning plus evening) spectra, and (b) the morning and evening limb spectra. Panel (c) shows the difference between the full limb spectra due to the disequilibrium thermochemistry, and panel (d) shows the difference between evening and morning limb spectra (evening minus morning). Faint grey dotted lines indicate the location of zero to better guide the eye.

inhomogeneities. von Paris et al. (2016) suggested inferring these inhomogeneities from transit light curves by modelling the signatures of morning and evening limbs imprinted onto these light curves as two stacked semicircles with different radii. This technique was later expanded upon by Espinoza & Jones (2021), who also performed a detailed study into the observational prospects of detecting limb in-

homogeneities with that technique when applied to observations with *TESS* and *JWST*. Espinoza & Jones (2021) reported that the asymmetry in the *JWST*/NIRISS/SOSS transit light curves is expected to be detectable for the evening-morning transit depth differences above ~25 ppm for a wide range of spectrophotometric precisions. Finally, Grant & Wakeford (2023) recently proposed another technique ca-

Figure 7. WASP-96b observed and simulated full limb (morning plus evening) transmission spectra. Transit depths observed with *VLT*/UT1/FORS2, *HST*/WFC3 G102 and G141, *Spitzer*/IRAC and *TESS* (Nikolov et al. 2022), *Magellan*/IMACS (McGruder et al. 2022) and *JWST*/NIRISS/SOSS (Radica et al. 2023) (the latter is shown at R≈125) are overlaid with the spectra predicted by the Met Office UNIFIED MODEL equilibrium and kinetics simulations assuming [M/H] = 0 or [M/H] = 1.

pable of inferring limb inhomogeneities from transit light curves, called transmission strings. This technique enables the extraction of transmission spectra not only for the morning and evening limbs separately, but also as a function of angle around a planet's terminator, i.e., planet's latitude. Latitudinally-resolved transmission spectra could be especially helpful for finding signs of species' quenching-driven equatorial depletion as well as of inhomogeneities in limbs' aerosol coverage. Overall, given the predictions from theory and the capabilities of existing observational techniques, there is potential for detecting evening-morning limb asymmetries in the atmosphere of WASP-96b and other similar planets.

If we compare H_2O, CO and CO_2 abundances retrieved from the *JWST*/NIRISS/SOSS transmission spectrum and assumed to be representative for the full limb of WASP-96b at $\sim 10^3 - 10^1$ Pa (Taylor et al. 2023) with H_2O, CO and CO_2 abundances predicted for the morning and evening limbs at $10^3 - 10^2$ Pa from our WASP-96b GCM simulations (Figs. A11-A13), we find that the retrieved H_2O abundance agrees better with H_2O abundances from our [M/H] = 0 simulations, while the retrieved CO_2 abundance agrees better with CO_2 abundances from our [M/H] = 1 simulations. The retrieved CO abundance was poorly constrained, resulting in its mean value agreeing better with CO abundances from our [M/H] = 0 simulations but not ruling out higher values consistent with our [M/H] = 1 simulations. This comparison suggests that given the limitations of their retrievals and our GCM, knowing H_2O, CO and CO_2 abundances might not be enough to constrain WASP-96b's atmospheric metallicity.

Putting our WASP-96b [M/H] = 0 kinetics simulation into context of previous similar studies (Drummond et al. 2020; Zamyatina et al. 2023), which, importantly, considered only [M/H] = 0, we find that our WASP-96b results are most similar to the results from their HD 189733b and HD 209458b [M/H] = 0 kinetics simulations. This is unsurprising as the WASP-96b system parameters are more similar to the system parameters of HD 189733b and HD 209458b than to those of HAT-P-11b and WASP-17b also present in Zamyatina

et al. (2023)'s planet sample. However, the differences between the system parameters of WASP-96b, HD 189733b and HD 209458b alter the predictions of CH_4, NH_3 and HCN quenching behaviour for these planets in such a way that puts WASP-96b's results somewhere in between those for HD 189733b and HD 209458b. For CH_4 specifically (Fig. A10), as the most spatially variable quenched species amongst CH_4, NH_3 and HCN in the case of these three planets, WASP-96b's meridional CH_4 quenching seems to be weaker than that of HD 189733b, causing WASP-96b's CH_4 abundances at $\leq 10^4$ Pa to be lower than those of HD 189733b but larger than those of HD 209458b. An investigation of the drivers of such differences is reserved for a future study.

Quenching is a well-known process in planetary sciences, especially after it was used to explain the discovery of CO in the upper atmosphere of Jupiter (Prinn & Barshay 1977). Since then many theoretical studies considered quenching by either performing chemical kinetics calculations or relying on the quenching approximation (e.g., Smith 1998; Line et al. 2010; Madhusudhan & Seager 2011; Visscher & Moses 2011; Zahnle & Marley 2014; Fortney et al. 2020; Soni & Acharyya 2023a,b). While such an approximation is simple and computationally efficient, the results obtained using this approximation often diverge from the chemical kinetics results for reasons discussed in detail in Tsai et al. (2017). Knowing that, we hope that our first demonstration of the variability in the quench level positions derived using a GCM coupled to a chemical kinetics scheme would encourage more studies similar to ours and benefit other modelling frameworks interested in quenching.

Aerosol formation in hot Jupiter atmospheres, and in particular formation of oxygen-bearing clouds, was estimated to be able to sequester up to 30% of oxygen from the entire atmosphere's gas phase under assumption of chemical equilibrium (Lee et al. 2016; Lee 2023). Such a depletion in oxygen would change the abundance and distribution of, e.g., H_2O and of elemental ratios such as C/O. The Helling et al. (2023) classification of gaseous exoplanets suggests that WASP-96b's C/O would be globally increased in cloud-forming

layers due to globally homogeneous cloud coverage. Given that their modelling framework relied on chemical equilibrium calculations for the gas-phase and our gas-phase only simulations did not include clouds, currently it is hard to predict how C/O would change if the gas-phase and cloud-phase chemical kinetics were coupled. Answering this question is one of the most challenging ongoing pursuits in exoplanet science.

5 CONCLUSIONS

We investigated the sensitivity of transport-induced quenching to an increase in atmospheric metallicity from [M/H] = 0 to [M/H] = 1 using 3D GCM simulations of an assumed to be aerosol-free hot Jupiter WASP-96b as an example. We found that:

- Quenching affects the spatial distribution of all chemical species, but species that quench zonally, e.g., CH_4, NH_3 and HCN, are affected by this process the most.
- The increase in atmospheric temperature at pressures $\sim 10^4$–10^7 Pa associated with an increase in atmospheric bulk metallicity could shift the location of the quench level to lower pressures, into the region of equatorial jet, and cause an equatorial depletion of species undergoing zonal quenching.
- The $\sim$3.0–5.0 µm region is the most powerful region in terms of evening-morning limb asymmetries for distinguishing atmospheres at chemical equilibrium from those with upper layers at thermochemical disequilibrium, and uniquely identifying their metallicity. This occurs because the amplitude and shape of evening-morning limb differences in that region are drastically different between our [M/H] = 0 and [M/H] = 1 equilibrium and kinetics simulations due to the difference in the abundance of H_2O and quenching behaviour of CO_2 and CH_4.

REFERENCES

Alam M. K., et al., 2021, The Astrophysical Journal, 906, L10
Amundsen D. S., et al., 2016, Astronomy & Astrophysics, 595, A36
Asplund M., Grevesse N., Sauval A. J., Scott P., 2009, Annual Review of Astronomy and Astrophysics, 47, 481
Baeyens R., Decin L., Carone L., Venot O., Agúndez M., Mollière P., 2021, Monthly Notices of the Royal Astronomical Society, 505, 5603
Burrows A., Sharp C. M., 1999, The Astrophysical Journal, 512, 843
Caffau E., Ludwig H. G., Steffen M., Freytag B., Bonifacio P., 2011, Solar Physics, 268, 255
Carone L., et al., 2020, Monthly Notices of the Royal Astronomical Society, 496, 3582
Christie D. A., et al., 2021, Monthly Notices of the Royal Astronomical Society, 506, 4500
Cooper C. S., Showman A. P., 2006, The Astrophysical Journal, 649, 1048
Dobbs-Dixon I., Agol E., 2013, Monthly Notices of the Royal Astronomical Society, 435, 3159
Drummond B., Tremblin P., Baraffe I., Amundsen D. S., Mayne N. J., Venot O., Goyal J., 2016, Astronomy & Astrophysics, 594, A69
Drummond B., Mayne N. J., Baraffe I., Tremblin P., Manners J., Amundsen D. S., Goyal J., Acreman D., 2018, Astronomy & Astrophysics, 612, A105
Drummond B., et al., 2020, Astronomy & Astrophysics, 636, A68
Ehrenreich D., et al., 2020, Nature, 580, 597
Espinoza N., Jones K., 2021, The Astronomical Journal, 162, 165
Fauchez T. J., et al., 2022, The Planetary Science Journal, 3, 213
Fortney J. J., Shabram M., Showman A. P., Lian Y., Freedman R. S., Marley M. S., Lewis N. K., 2010, The Astrophysical Journal, 709, 1396
Fortney J. J., Visscher C., Marley M. S., Hood C. E., Line M. R., Thorngren D. P., Freedman R. S., Lupu R., 2020, The Astronomical Journal, 160, 288
Goyal J. M., et al., 2020, Monthly Notices of the Royal Astronomical Society, 498, 4680
Grant D., Wakeford H. R., 2023, Monthly Notices of the Royal Astronomical Society, 519, 5114
Harris C. R., et al., 2020, Nature, 585, 357
Hattersley R., et al., 2023, SciTools/iris, doi:10.5281/zenodo.8305232
Hedges C., Madhusudhan N., 2016, Monthly Notices of the Royal Astronomical Society, 458, 1427
Hellier C., et al., 2014, Monthly Notices of the Royal Astronomical Society, 440, 1982
Helling C., Kawashima Y., Graham V., Samra D., Chubb K. L., Min M., Waters L. B., Parmentier V., 2020, Astronomy & Astrophysics, 641, A178
Helling C., et al., 2023, Astronomy & Astrophysics, 671, A122
Hunter J. D., 2007, Computing in Science & Engineering, 9, 90
Kempton E. M.-R., Bean J. L., Parmentier V., 2017, The Astrophysical Journal Letters, 845, L20
Kesseli A. Y., Snellen I. A. G., Casasayas-Barris N., Mollière P., Sánchez-López A., 2022, The Astronomical Journal, 163, 107
Kluyver T., et al., 2016, in Loizides F., Scmidt B., eds, Positioning and

Power in Academic Publishing: Players, Agents and Agendas - Proceedings of the 20th International Conference on Electronic Publishing. IOS Press, pp 87–90, doi:10.3233/978-1-61499-649-1-87, https://eprints.soton.ac.uk/403913/

Komacek T. D., Gao P., Thorngren D. P., May E. M., Tan X., 2022, The Astrophysical Journal Letters, 941, L40

Lee E. K. H., 2023, Monthly Notices of the Royal Astronomical Society, 524, 2918

Lee G., Dobbs-Dixon I., Helling C., Bognar K., Woitke P., 2016, Astronomy & Astrophysics, 594, A48

Lee E. K., Parmentier V., Hammond M., Grimm S. L., Kitzmann D., Tan X., Tsai S. M., Pierrehumbert R. T., 2021, Monthly Notices of the Royal Astronomical Society, 506, 2695

Lee E. K., Tsai S.-M., Hammond M., Tan X., 2023, Astronomy & Astrophysics, 672, A110

Line M. R., Parmentier V., 2016, The Astrophysical Journal, 820, 78

Line M. R., Liang M. C., Yung Y. L., 2010, The Astrophysical Journal, 717, 496

Lines S., et al., 2018, Monthly Notices of the Royal Astronomical Society, 481, 194

Lodders K., Fegley B. J., 2002, Icarus, 155, 393

Lodders K., Palme H., Gail H.-P., 2009, in Trümper J. E., ed., , Vol. 4B, Solar System. SpringerMaterials, doi:10.1007/978-3-540-88055-4_34, http://materials.springer.com/lb/docs/sm_lbs_978-3-540-88055-4_34

MacDonald R. J., Goyal J. M., Lewis N. K., 2020, The Astrophysical Journal Letters, 893, L43

Madhusudhan N., Seager S., 2011, The Astrophysical Journal, 729, 41

Mayne N. J., et al., 2014, Astronomy & Astrophysics, 561, A1

Mayne N. J., et al., 2017, Astronomy & Astrophysics, 604, A79

McGruder C. D., et al., 2022, The Astronomical Journal, 164, 134

Mendonça J. M., Grimm S. L., Grosheintz L., Heng K., 2016, The Astrophysical Journal, 829, 115

Menou K., 2020, Monthly Notices of the Royal Astronomical Society, 493, 5038

Moses J. I., 2014, Philosophical Transactions of the Royal Society A: Mathematical, Physical and Engineering Sciences, 372

Moses J. I., et al., 2011, The Astrophysical Journal, 737

Moses J. I., Tremblin P., Venot O., Miguel Y., 2022, Experimental Astronomy, 53, 279–322

Nikolov N., et al., 2018, Nature, 557, 526

Nikolov N. K., et al., 2022, Monthly Notices of the Royal Astronomical Society, 515, 3037–3058

Perez F., Granger B. E., 2007, Computing in Science & Engineering, 9, 21

Pluriel W., 2023, Remote Sensing, 15, 635

Pontoppidan K. M., et al., 2022, The Astrophysical Journal Letters, 936, L14

Powell D., Louden T., Kreidberg L., Zhang X., Gao P., Parmentier V., 2019, The Astrophysical Journal, 887, 170

Prinn R. G., Barshay S. S., 1977, Science, 198, 1031

Prinoth B., et al., 2022, Nature Astronomy, 6, 449

Radica M., et al., 2023, Monthly Notices of the Royal Astronomical Society, 524, 835

Rajpurohit A. S., Reylé C., Allard F., Homeier D., Schultheis M., Bessell M. S., Robin A. C., 2013, Astronomy & Astrophysics, 556, A15

Rauscher E., Menou K., 2010, The Astrophysical Journal, 714, 1334

Rustamkulov Z., et al., 2023, Nature, 614, 659

Sainsbury-Martinez F., et al., 2019, Astronomy & Astrophysics, 632, A114

Samra D., Helling C., Chubb K. L., Min M., Carone L., Schneider A. D., 2023, Astronomy & Astrophysics, 669, A142

Savel A. B., Kempton E. M.-R., Rauscher E., Komacek T. D., Bean J. L., Malik M., Malsky I., 2023, The Astrophysical Journal, 944, 99

Sergeev D. E., Zamyatina M., 2023, Aeolus - a Python library for the analysis and visualisation of climate model output, doi:10.5281/zenodo.8370384

Showman A. P., Fortney J. J., Lian Y., Marley M. S., Freedman R. S., Knutson H. A., Charbonneau D., 2009, The Astrophysical Journal, 699, 564

Showman A. P., Tan X., Parmentier V., 2020, Space Science Reviews, 216, 139

Smith M. D., 1998, Icarus, 132, 176

Soni V., Acharyya K., 2023a, The Astrophysical Journal, 946, 29

Soni V., Acharyya K., 2023b, The Astrophysical Journal, 958, 143

Steinrueck M. E., Showman A. P., Lavvas P., Koskinen T., Tan X., Zhang X., 2021, Monthly Notices of the Royal Astronomical Society, 504, 2783

Taylor J., et al., 2023, Monthly Notices of the Royal Astronomical Society, 524, 817

Tremblin P., Amundsen D. S., Mourier P., Baraffe I., Chabrier G., Drummond B., Homeier D., Venot O., 2015, The Astrophysical Journal Letters, 804, L17

Tremblin P., et al., 2017, The Astrophysical Journal, 841, 30

Tsai S.-M., Lyons J. R., Grosheintz L., Rimmer P. B., Kitzmann D., Heng K., 2017, The Astrophysical Journal Supplement Series, 228, 20

Tsai S.-M., Lee E. K. H., Pierrehumbert R., 2022, Astronomy & Astrophysics, 664, A82

Tsai S.-M., Moses J. I., Powell D., Lee E. K. H., 2023, The Astrophysical Journal Letters, 959, L30

Venot O., Hébrard E., Agúndez M., Dobrijevic M., Selsis F., Hersant F., Iro N., Bounaceur R., 2012, Astronomy & Astrophysics, 546, A43

Venot O., Bounaceur R., Dobrijevic M., Hébrard E., Cavalié T., Tremblin P., Drummond B., Charnay B., 2019, Astronomy & Astrophysics, 624, A58

Visscher C., Moses J. I., 2011, The Astrophysical Journal, 738, 72

Welbanks L., Madhusudhan N., Allard N. F., Hubeny I., Spiegelman F., Leininger T., 2019, The Astrophysical Journal Letters, 887, L20

Yip K. H., Changeat Q., Edwards B., Morvan M., Chubb K. L., Tsiaras A., Waldmann I. P., Tinetti G., 2021, The Astronomical Journal, 161, 4

Zahnle K. J., Marley M. S., 2014, The Astrophysical Journal, 797, 41

Zamyatina M., et al., 2023, Monthly Notices of the Royal Astronomical Society, 519, 3129

von Paris P., Gratier P., Bordé P., Leconte J., Selsis F., 2016, Astronomy & Astrophysics, 589, A52

APPENDIX A: APPENDIX

Figures in this section provide additional information about our GCM simulations: Fig. A1-A2 — conservation and steady state diagnostics, Fig. A3 — zonal-mean zonal wind speeds, Fig. A4 — vertical pressure-temperature profiles in the terminator plane, Figs. A5-A9 — the distribution of NH_3, HCN, CO_2, H_2O and CO in the terminator plane, Figs. A10-A15 — vertical profiles of CH_4, CO, CO_2, H_2O, HCN and NH_3, Fig. A16 — the contributions of CH_4, CO, CO_2, H_2O, HCN and NH_3 to the full limb transmission spectra and Fig. A17 — the morning and evening limb transmission spectra shown on separate panels.

This paper has been typeset from a TEX/LATEX file prepared by the author.
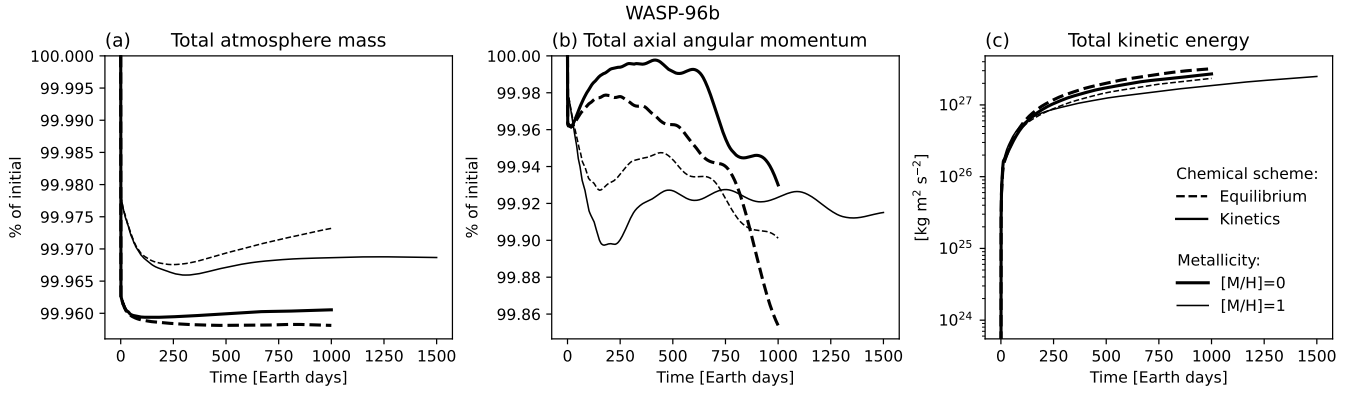
Figure A1. Conservation diagnostics from the WASP-96b equilibrium and kinetics simulations assuming [M/H] = 0 or [M/H] = 1.
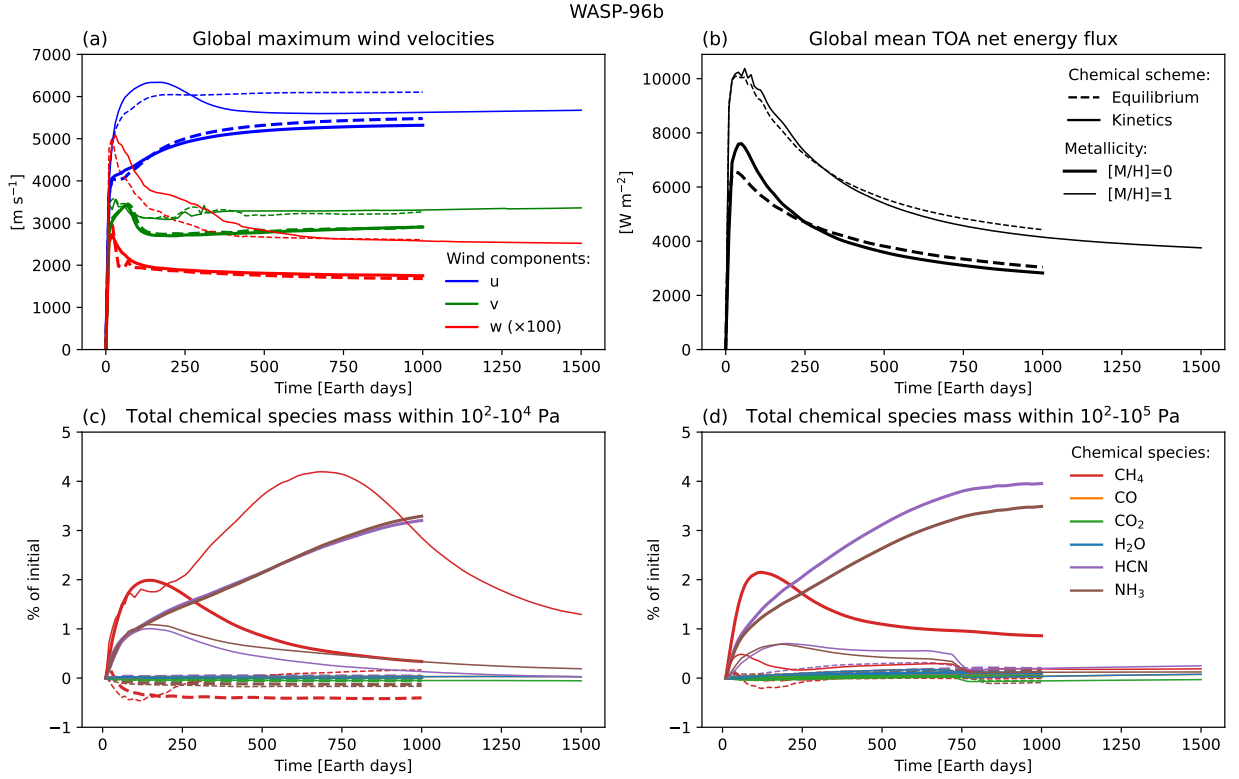
Figure A2. Steady state diagnostics from the WASP-96b equilibrium and kinetics simulations assuming [M/H] = 0 or [M/H] = 1. All panels share the legend of panel (b), and panels (c) and (d) share the legend of panel (d). Simulations approached the dynamical (a), radiative (b) and chemical (c)-(d) pseudo-steady state. The kinetics simulation with [M/H] = 1 was run for longer (1500 Earth days) to better stabilise the total CH_4 mass within 10^2-10^4 Pa.
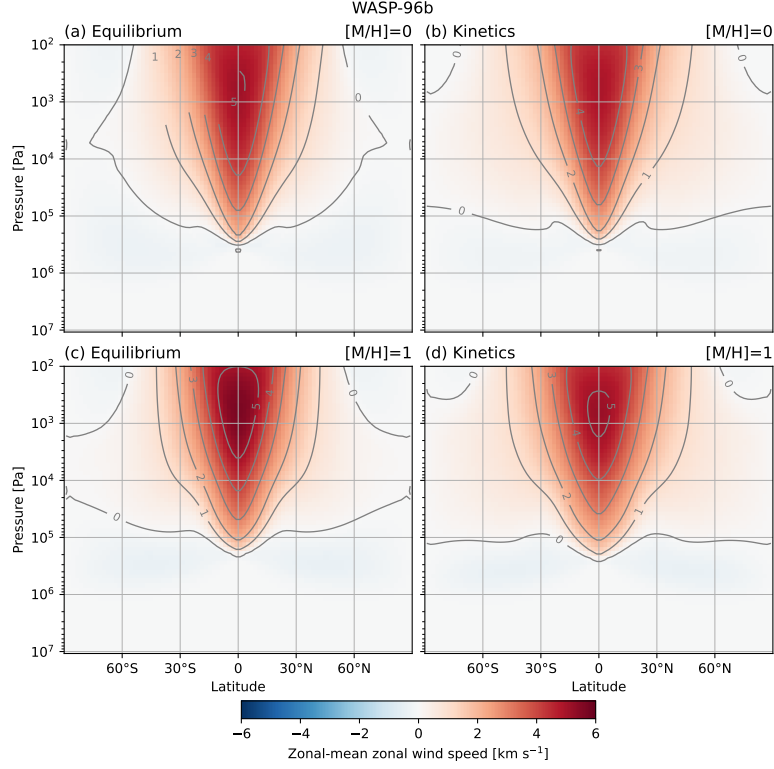
Figure A3. Zonal-mean zonal wind speeds from the WASP-96b equilibrium and kinetics simulations assuming [M/H] = 0 or [M/H] = 1. Simulations with a higher metallicity predict faster zonal-mean zonal wind speeds, but the general jet structure is similar in all simulations.
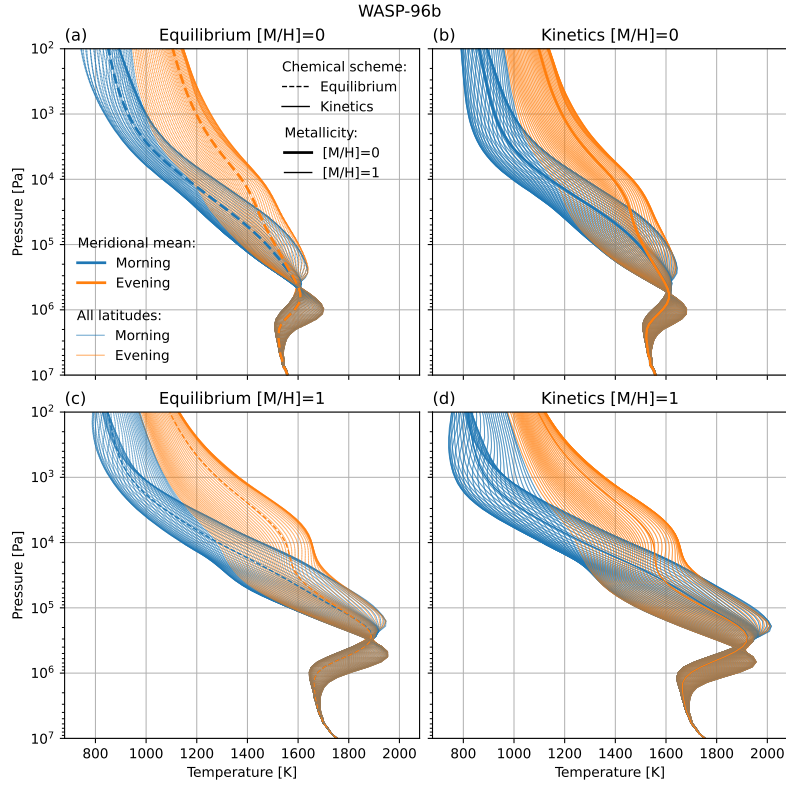
Figure A4. Pressure-temperature vertical profiles at the morning and evening limb from the WASP-96b equilibrium and kinetics simulations assuming [M/H] = 0 or [M/H] = 1.
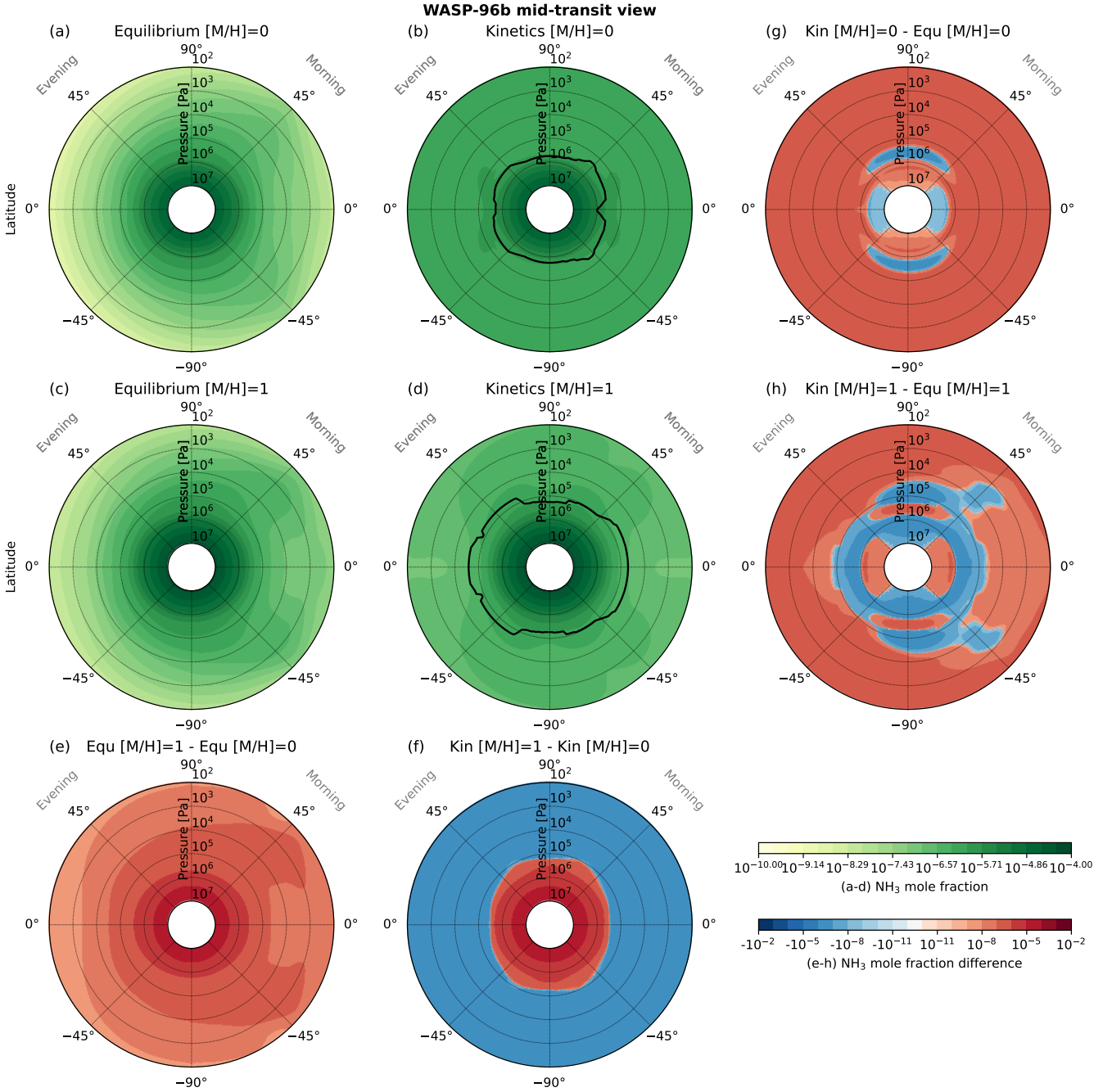
Figure A5. As in Fig. 4 but for NH₃.
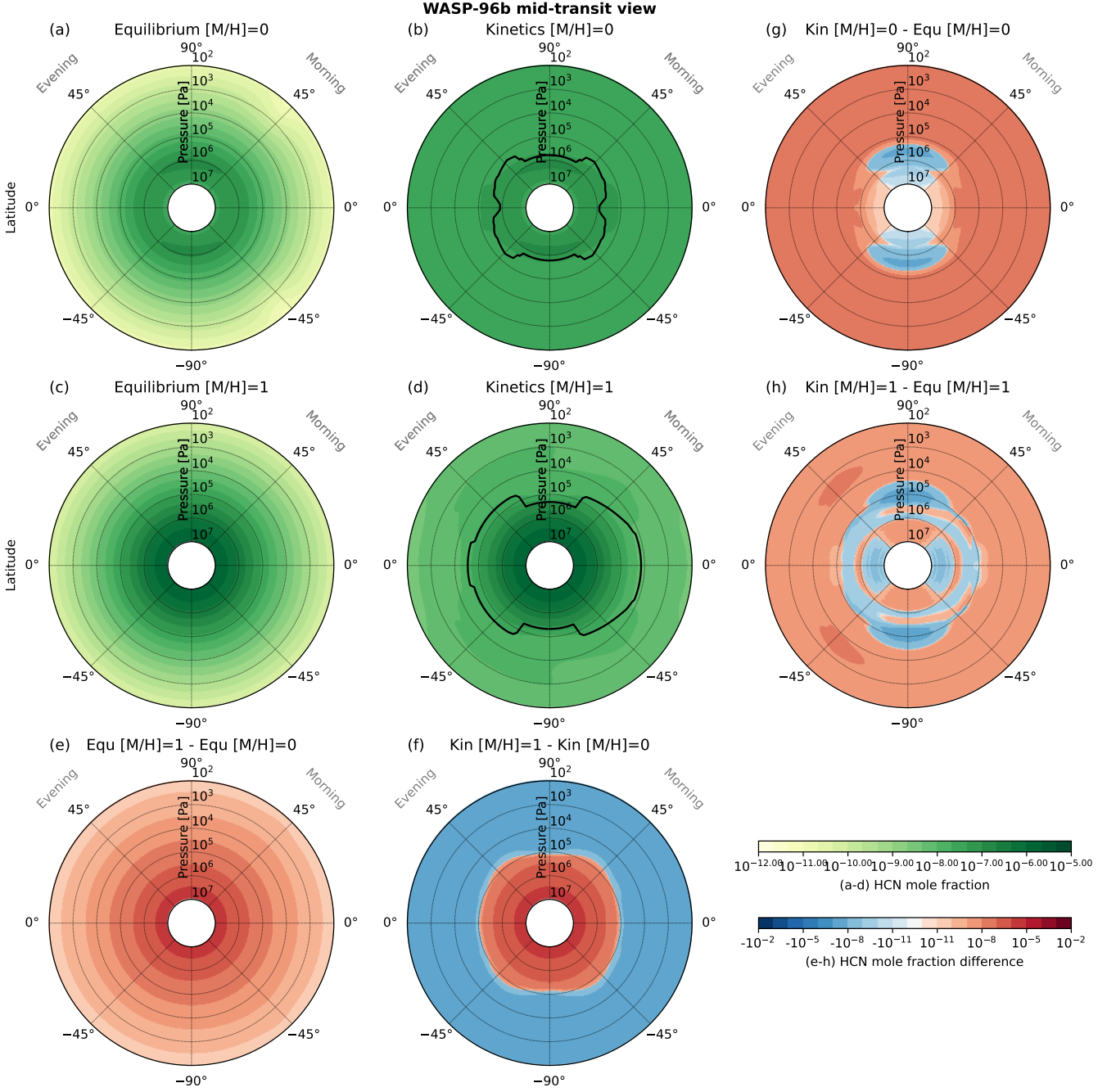
Figure A6. As in Fig. 4 but for HCN.
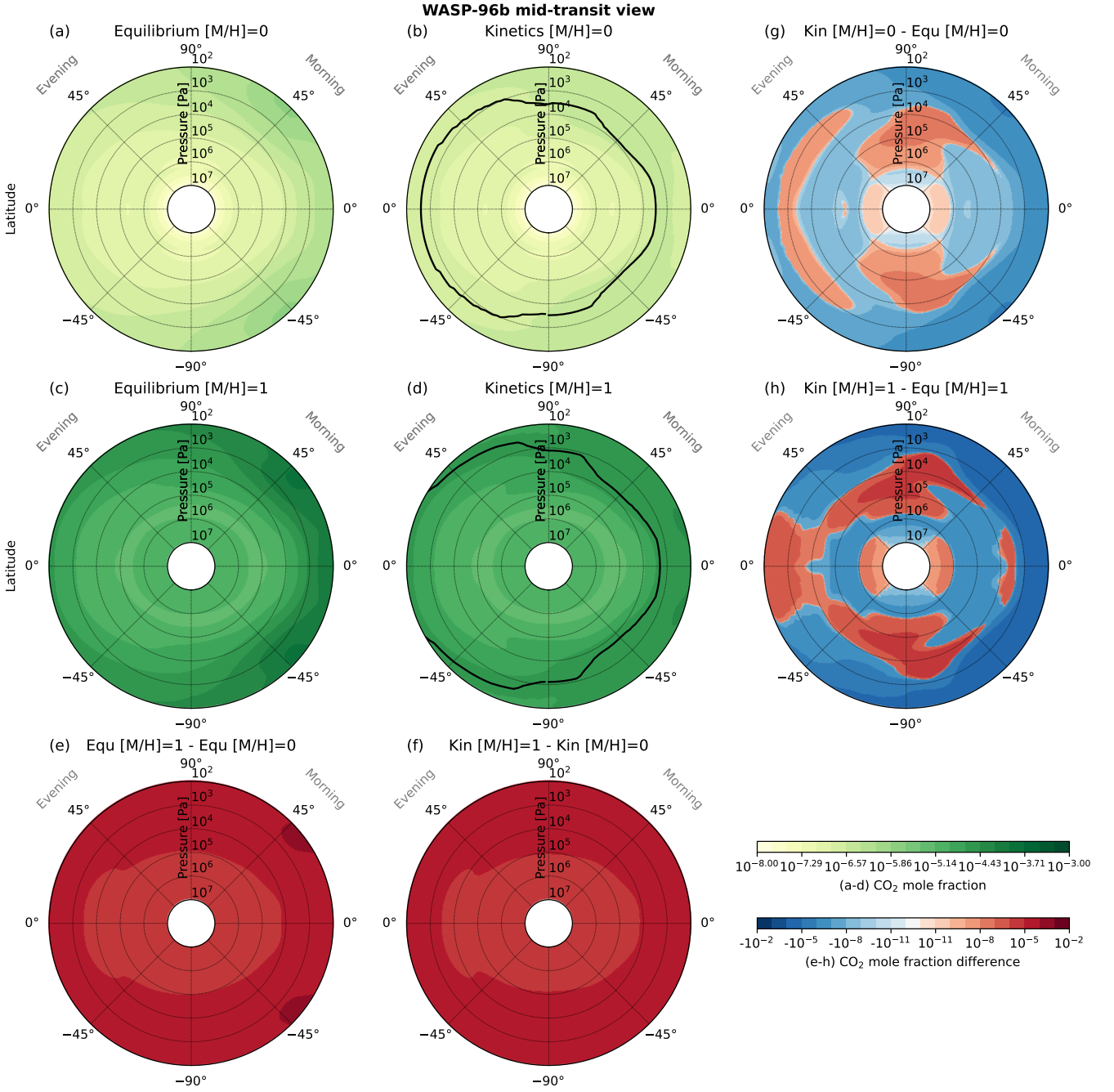
Figure A7. As in Fig. 4 but for CO$_2$.
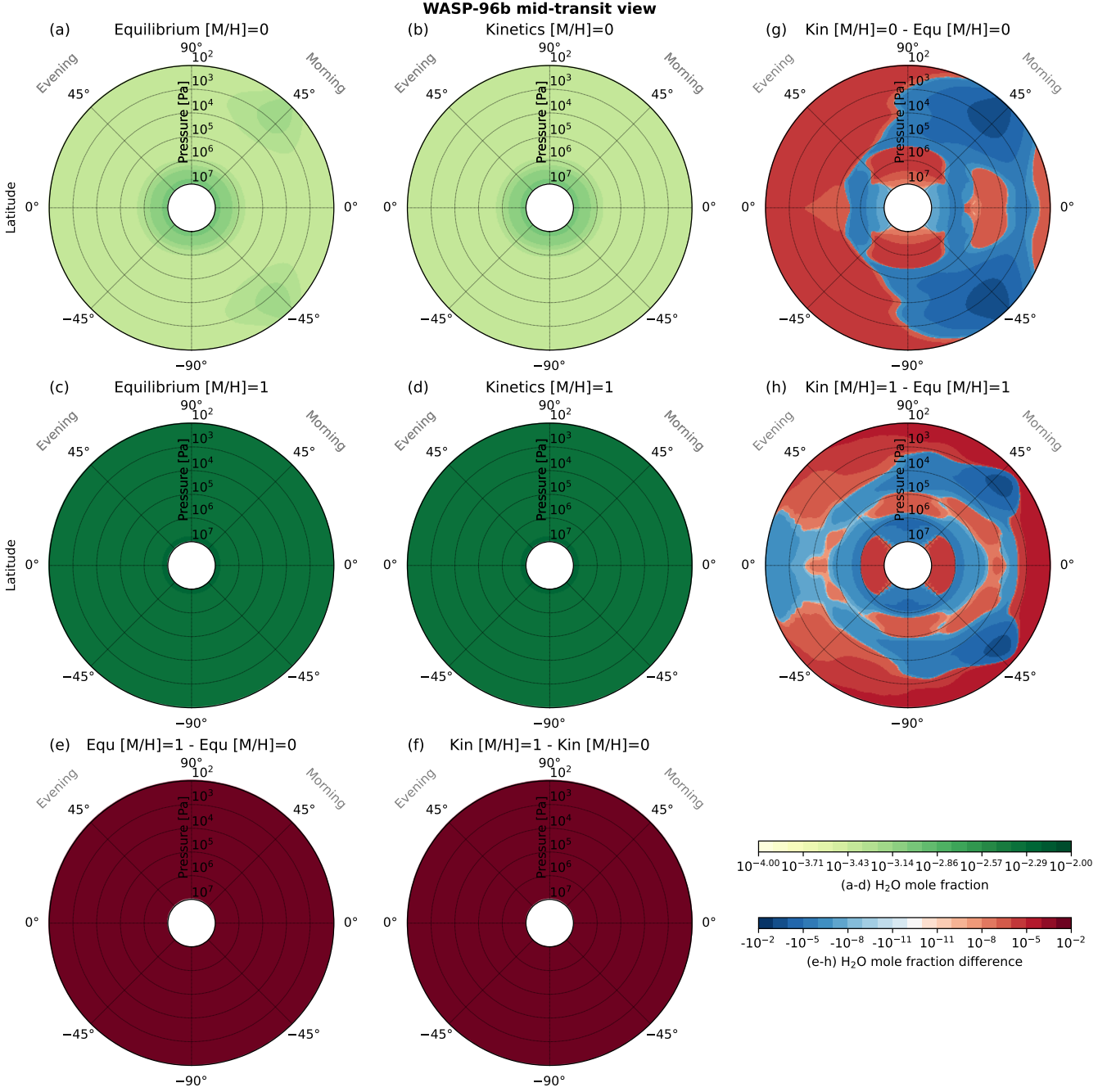
Figure A8. As in Fig. 4 but for H_2O.

WASP-96b mid-transit view
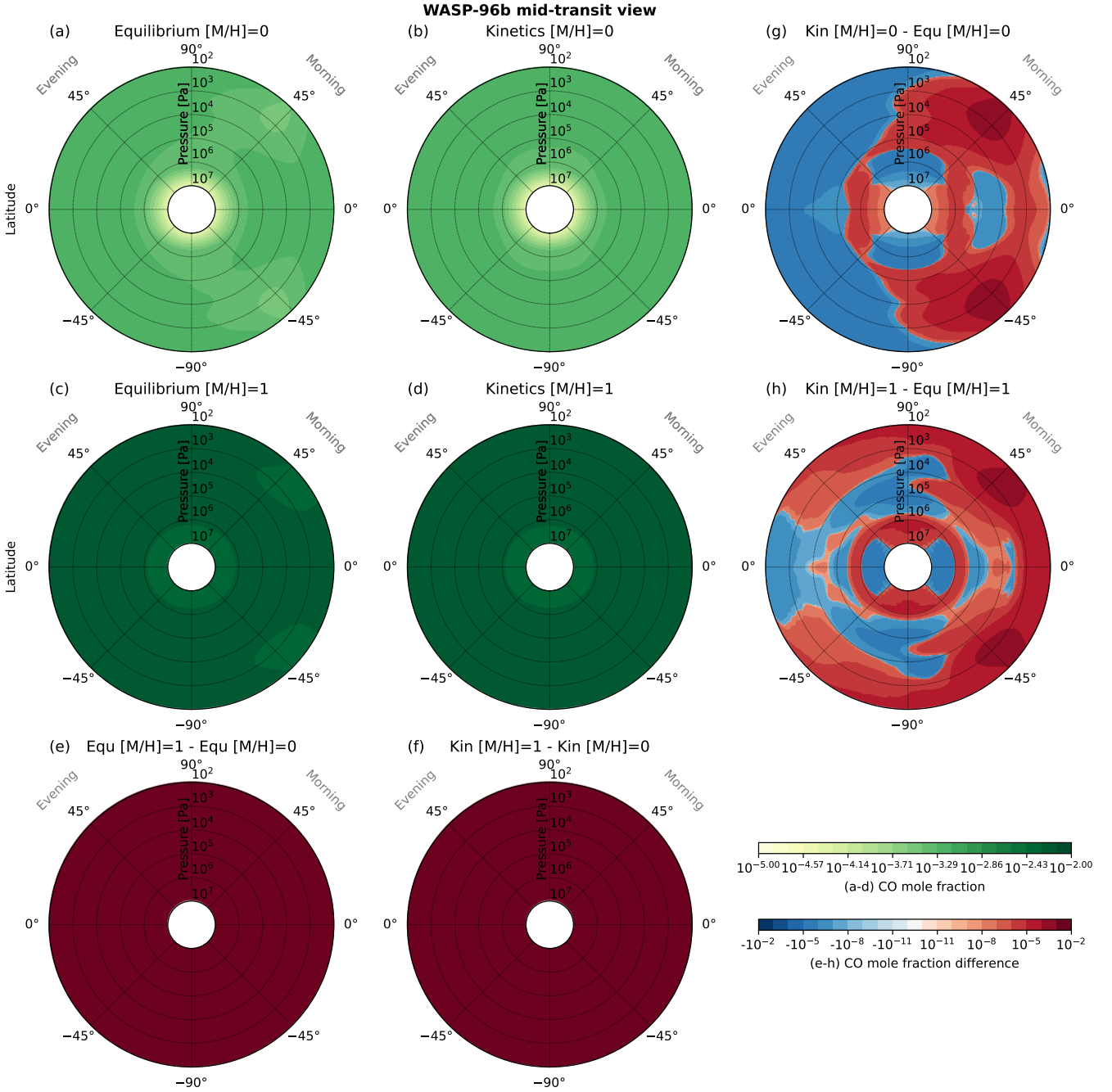

Figure A9. As in Fig. 4 but for CO.
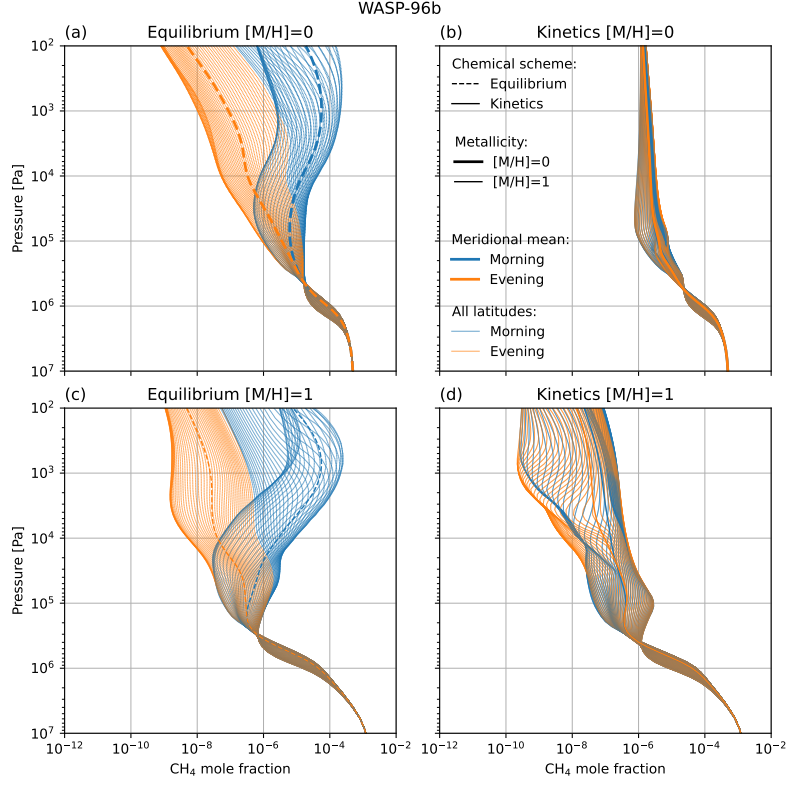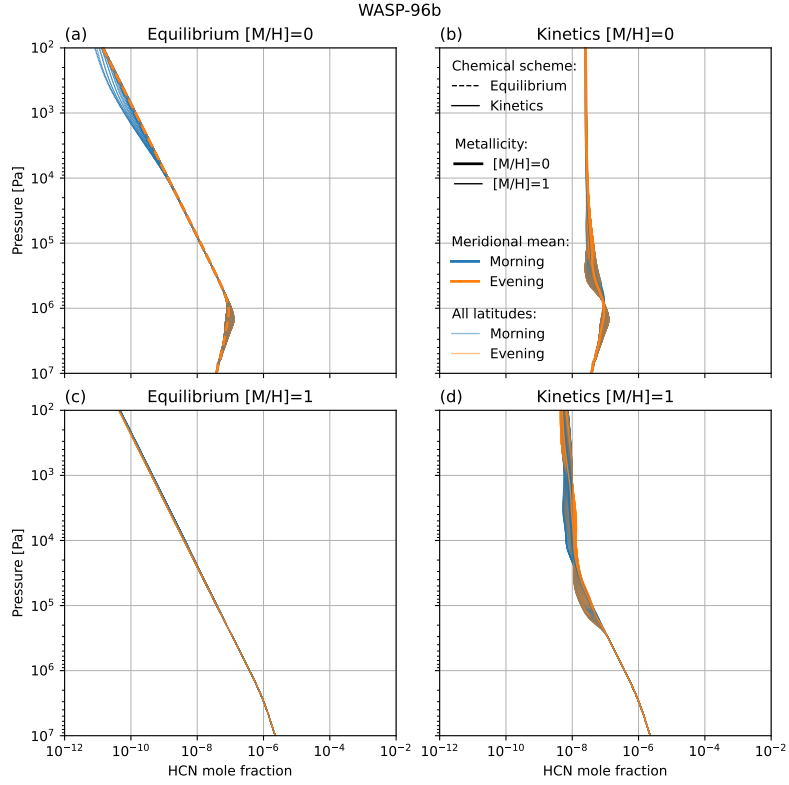
Figure A10. As in Fig. A4 but for CH$_4$ mole fraction.
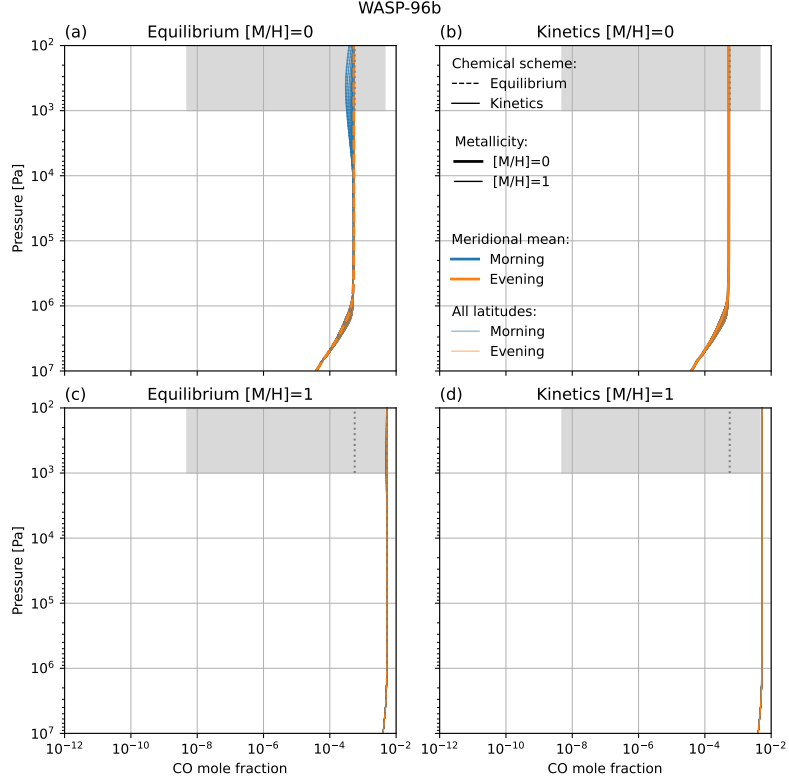
Figure A11. As in Fig. A4 but for CO mole fraction. CO abundance and its 1σ uncertainty, $\log_{10}$(CO) = $-3.25^{+0.91}_{-5.06}$, recovered using the free retrieval code Aurora in Taylor et al. (2023) are shown as a grey dotted line and grey shading, respectively.
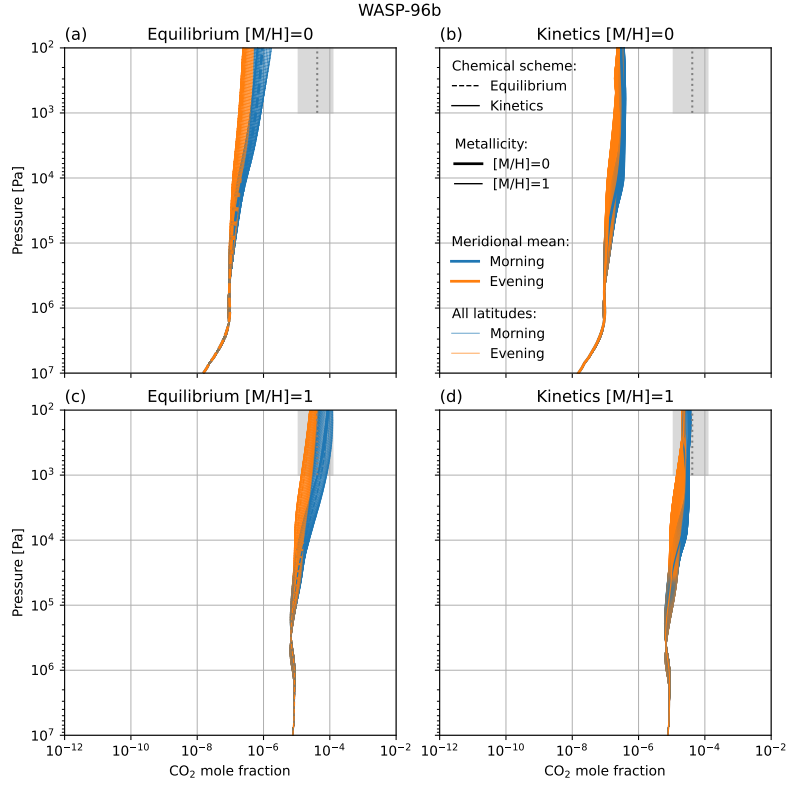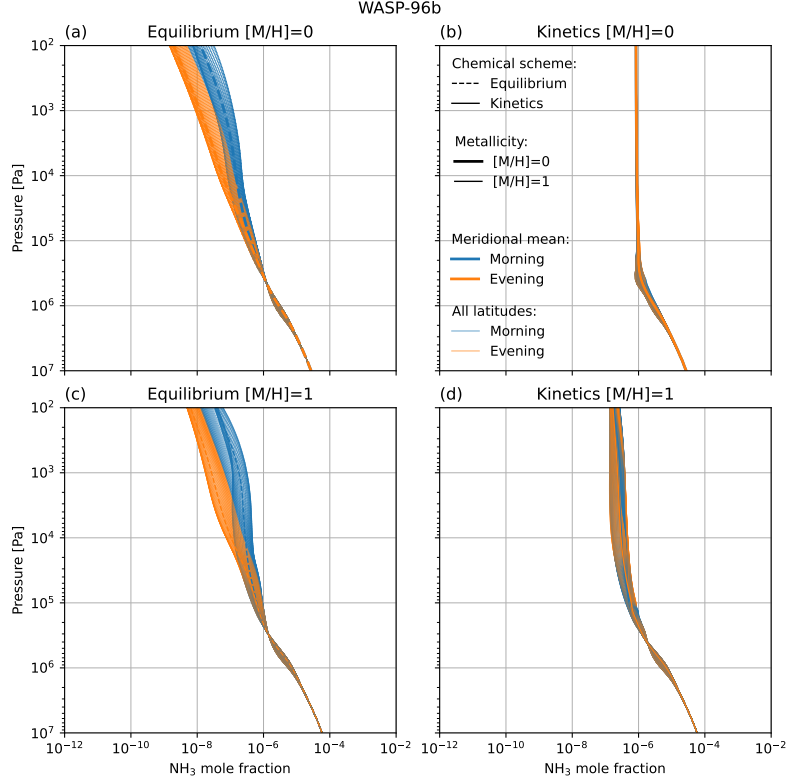
Figure A12. As in Fig. A4 but for CO_2 mole fraction. CO_2 abundance and its 1σ uncertainty, $\log_{10}(CO_2) = -4.38^{+0.47}_{-0.57}$, recovered using the free retrieval code Aurora in Taylor et al. (2023) are shown as a grey dotted line and grey shading, respectively.
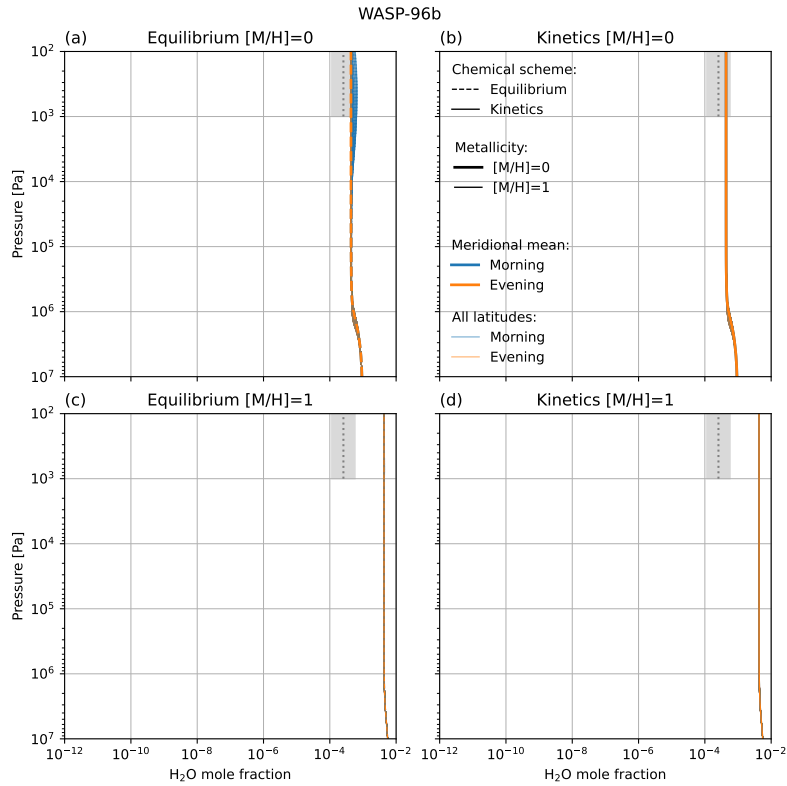
Figure A13. As in Fig. A4 but for H_2O mole fraction. H_2O abundance and its 1σ uncertainty, $\log_{10}(H_2O) = -3.59^{+0.35}_{-0.35}$, recovered using the free retrieval code Aurora in Taylor et al. (2023) are shown as a grey dotted line and grey shading, respectively.
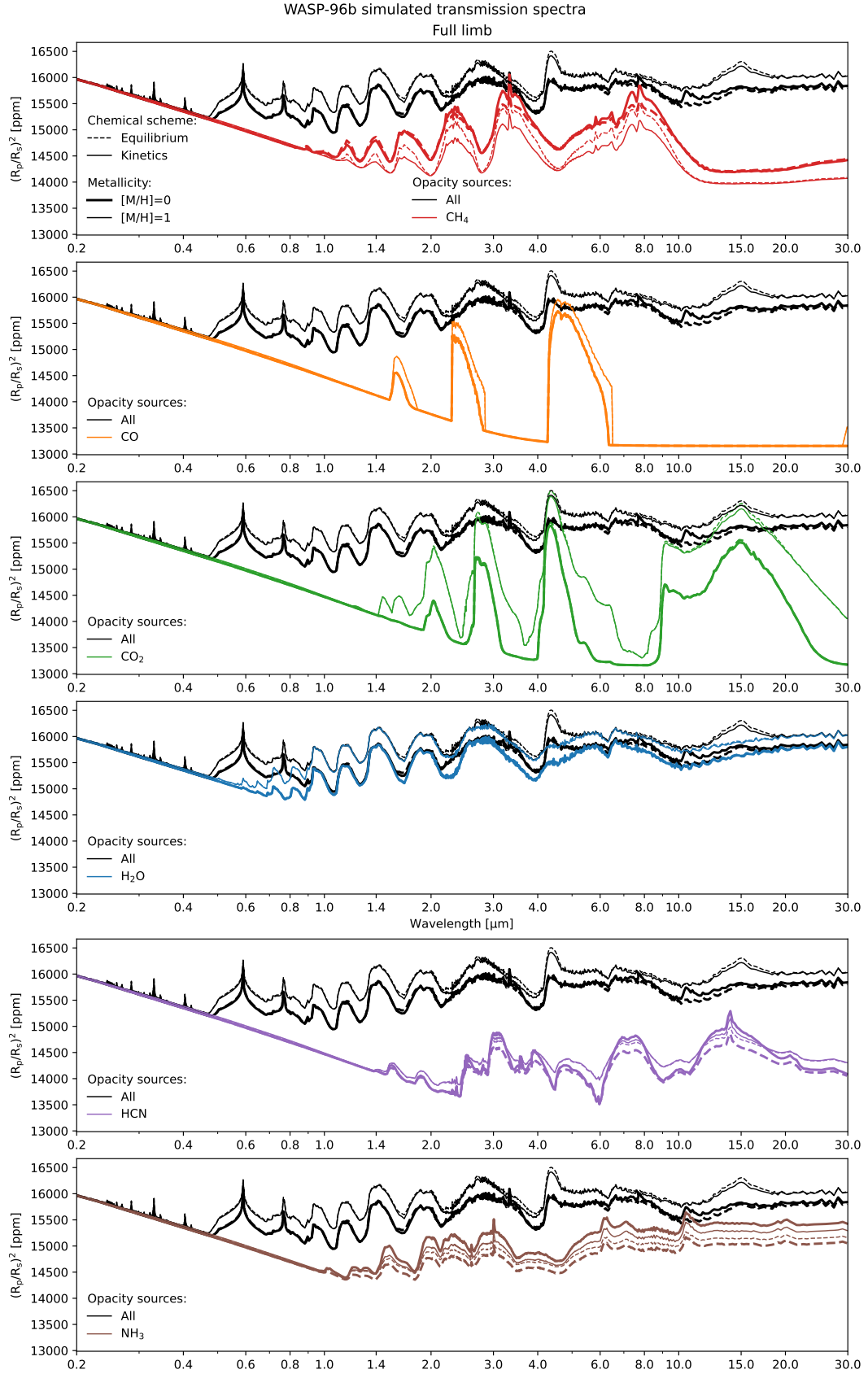
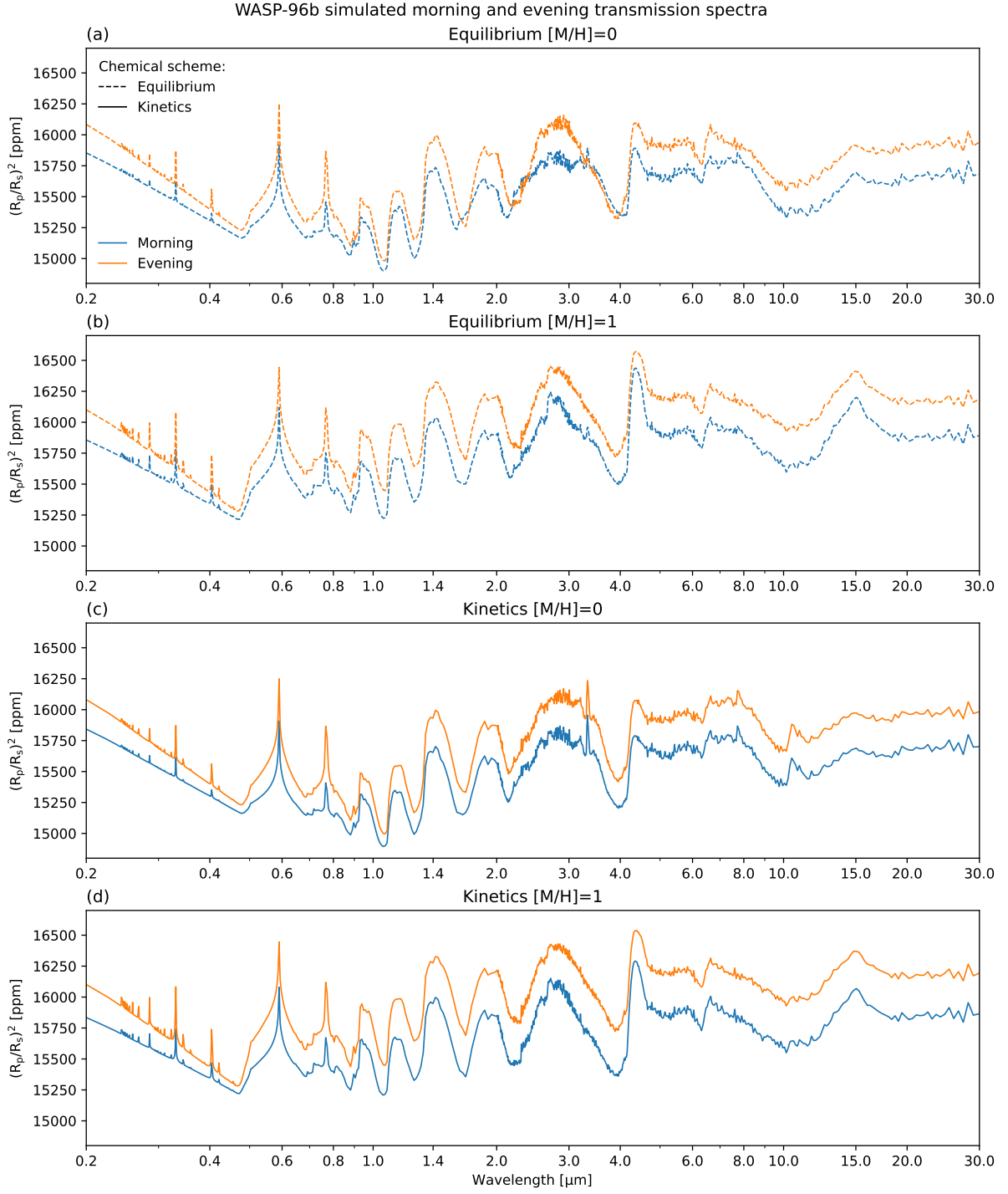**Figure A14.** As in Fig. A4 but for HCN mole fraction.

Figure A15. As in Fig. A4 but for NH$_3$ mole fraction.

Figure A16. Contributions of CH_4, CO, CO_2, H_2O, HCN and NH_3 to the full limb transmission spectra from the WASP-96b equilibrium and kinetics simulations assuming [M/H] = 0 or [M/H] = 1.

Figure A17. As in Fig.6b but showing the morning and evening limb transmission spectra on separate panels.